Physico-chemical modeling of the First Aerosol Characterization Experiment (ACE 1) Lagrangian B
1. A moving column approach

Karsten Suhre,[1] Céline Mari,[1] Timothy S. Bates,[2] James E. Johnson,[2]
Robert Rosset,[1] Qing Wang,[3] Alan R. Bandy,[4] Donald R. Blake,[5]
Steven Businger,[6] Fred L. Eisele,[7] Barry J. Huebert,[8] Gregory L. Kok,[9]
R. Lee Mauldin III,[7] André S. H. Prévôt,[9,10] Richard D. Schillawski,[9]
David J. Tanner,[7] and Donald C. Thornton[4]

Abstract. During Lagrangian experiment B (LB in the following) of the First Aerosol Characterization Experiment (ACE 1), a clean maritime air mass was followed over a period of 28 hours. During that time span, the vertical distribution of aerosols and their gas phase precursors were characterized by a total of nine aircraft soundings which were performed during three research flights that followed the trajectory of a set of marked tetroons. The objective of this paper is to study the time evolution of gas phase photochemistry in this Lagrangian framework. A box model approach to the wind shear driven and vertically stratified boundary layer is questionable, since its basic assumption of instantaneous turbulent mixing of the entire air column is not satisfied here. To overcome this obstacle, a one-dimensional Lagrangian boundary layer meteorological model with coupled gas phase photochemistry is used. To our knowledge, this is the first time that such a model is applied to a Lagrangian experiment and that enough measurements are available to fully constrain the simulations. A major part of this paper is devoted to the question of to what degree our model is able to reproduce the time evolution and the vertical distribution of the observed species. Comparison with observations of O_3, OH, H_2O_2, CH_3OOH, DMS, and CH_3I, made on the nine Lagrangian aircraft soundings shows that this is in general the case, although the dynamical simulation started to deviate from the observations on the last Lagrangian flight. In agreement with experimental findings reported by Q. Wang et al. (unpublished manuscript, 1998b), generation of turbulence in the model appears to be most sensitive to the imposed sea surface temperature. Concerning the different modeled and observed chemical species, a number of conclusions are drawn: (1) Ozone, having a relatively long photochemical lifetime in the clean marine boundary layer, is found to be controlled by vertical transport processes, in particular synoptic-scale subsidence or ascent. (2) Starting with initally constant vertical profiles, the model is able to "create" qualitatively the vertical structure of the observed peroxides. (3) OH concentrations are in agreement with observations, both on cloudy and noncloudy days. On the first flight, a layer of dry ozone rich air topped the boundary layer. The model predicts a minimum in OH and peroxides at that altitude consistent with observations. (4) Atmospheric DMS concentrations are modeled correctly only when using the *Liss and Merlivat* [1986] flux parameterization, the *Wanninkhof* [1992] flux parameterization giving values twice those observed. To arrive at this conclusion, OH is assumed to be the major DMS oxidant, but no assumptions about mixing heights or entrainment rates are necessary in this type of model. DMS seawater concentrations are constrained by observations.

[1]Laboratoire d'Aérologie, UMR CNRS/Université Paul Sabatier, Toulouse, France.

[2]Pacific Marine Environmental Laboratory, NOAA, Seattle, Washington.

[3]Naval Postgraduate School, Monterey, California.

[4]Department of Chemistry, Drexel University, Philadelphia, Pennsylvania.

[5]Department of Chemistry, University of California at Irvine.

[6]Department of Meteorology, University of Hawai'i at Mānoa.

[7]Atmospheric Chemistry Division, National Center for Atmospheric Research, Boulder, Colorado.

[8]Department of Oceanography, University of Hawai'i at Mānoa.

[9]Research Aviation Facility, National Center for Atmospheric Research, Boulder, Colorado.

[10]Paul Scherrer Institute, Villigen, Switzerland.

1. Introduction

The basic problem in all studies of atmospheric physico-chemical processes is the complex interplay between a large number of mutually dependant variables, making investigation of individual components of the system difficult. The objective of atmospheric physico-chemical modeling is to conceive numerical models and parameterizations that are able to reproduce experimental observations at the best possible level. If this approach is successful for a given problem, it can be assumed that the underlying processes are understood. In that case, such a model can then be used to execute a number of sensitivity studies, for example, to assess parameters inaccessible to direct measurements and to determine the relative contribution of different processes to an overall phenomenon. Improvement of numerical models relies strongly on experimental field campaigns that are designed to match the models' needs.

In this work we apply a one-dimensional (1-D) physico-chemical Lagrangian model of the cloudy marine boundary layer (MBL) to the comprehensive data set collected during the Lagrangian experiment B (LB in the following) of the International Global Atmospheric Chemistry (IGAC) First Aerosol Characterization Experiment (ACE 1) [*Bates et al.*, this issue (a)]. The concept of such a Lagrangian experiment is inherently adapted to the application of a Lagrangian column model, since both the model as well as the experimental strategy assume horizontal homogeneity in the observed and simulated variables and both describe the vertical structure of the MBL in great detail. The dynamical part of our model prognostically calculates the evolution of wind speed, temperature, humidity, cloud water content, and turbulent kinetic energy. The basic physico-chemical processes that are treated are sea-air emission, turbulent mixing, synoptic-scale subsidence or ascent, photochemistry, and dry deposition to the ocean surface. We compare our model in particular with data collected during nine aircraft soundings from flights 24-26. These flights followed the path of a set of three smart marker tetroons released from the Research Vessel (R/V) *Discoverer* [*Businger et al.*, 1996, also unpublished manuscript, 1998] and monitored the same air mass over a 28 hour period. Vertical profiles of dimethyl sulfide (DMS) and methyl iodide (CH$_3$I) are used to focus in particular on sea-air emission fluxes, hydrogen peroxide (H$_2$O$_2$) and methylhydroperoxide (CH$_3$OOH) for dry deposition, the hydroxyl radical (OH) for photochemistry, including the effect of clouds on photolysis rates, and ozone (O$_3$) for vertical turbulent transport and entrainment. In this context, ACE 1 LB may be viewed as a two-dimensional (time-height) closure experiment [*Quinn et al.*, 1996], where the independant variables are the different parameters that go into the forcing of the column model, that is the initial dynamical and chemical profiles, the synoptic-scale subsidence or ascent, the geostrophic wind, and the variation of sea surface temperature and seawater DMS concentration.

The dependant variables are the time-height distributions of the different chemical species. Only gas phase chemistry is treated at this point, which is justified by the fact that the first two Lagrangian flights took place under mostly noncloudy conditions and that with the exception of the peroxides, all chemical species we focus on here are mostly unsoluble.

What is the interest of using a 1-D column model rather than a simple zero-dimensional box model? Applied to a Lagrangian experiment, a box model by construction represents a well mixed MBL, the model variables being interpreted as average MBL quantities. The basic assumption is that turbulent mixing takes places instantaneously so that no vertical gradients in chemical species can be represented. The boundary layer encountered in LB, in contrast, was mainly stably stratified, with weak wind shear driven turbulence in the beginning that increased toward the end of LB, as wind speed increased and clouds developed. A distinct two layer structure was observed for a number of dynamical and chemical variables, that is, potential temperature, water vapor mixing ratio, ozone, and peroxides. Moreover, in a box model a number of physical processes can only be coarsely parameterized, that is, entrainment of free tropospheric air, cloud cycling, sea-air and dry deposition fluxes, and vertical dependance of photolysis rates on the cloud profile. A column model, in contrast, prognostically calculates the evolution of the MBL based on physical parameterizations, in particular the vertical structure of turbulence, cloud profiles, radiative and actinic fluxes, surface winds, etc. Reaction rates are functions of height, dependant on temperature, pressure and humidity. Entrainment is calculated prognostically as the difference between the turbulent boundary layer growth and an imposed synoptic-scale subsidence or ascent. Still, a 1-D model is only moderately expensive in terms of computing time (about 50 times that of a box model: here, 1.5 min CPU time for 1 hour of simulation on a Cray J90) as compared to a fully three-dimensional chemistry transport model (about 100,000 times that of a box model, assuming a small 50x50x40 grid).

The present work is to our knowledge the first time that a Lagrangian one-dimensional boundary layer meteorological model with coupled photochemistry is applied to a Lagrangian experiment that includes enough measurements to fully constrain such a model. Thus one major objective of this paper is to investigate to what degree our model is able to reproduce the evolution of O$_3$, OH, peroxides, DMS, CH$_3$I, and other reactive species in the marine boundary layer. If the model approach proves successful, it will be possible to implement in the future relatively complex aerosol models into the 1-D framework, making it a useful tool for the study of processes linked to direct and indirect radiative forcing by aerosols and processes concerning heterogeneous chemistry in aerosols and cloud droplets, especially in the context of future Lagrangian experiments

in ACE 2. In a companion paper [*Mari et al.*, this issue], the same mesoscale meteorological model is applied in its three-dimensional configuration in order to study the interaction between the different processes that control DMS in the atmosphere, that is, emission, turbulent and advective transport, and oxidation. A third paper (C. Mari et al., manuscript in preparation, 1998) will eventually address issues not treated here, in particular modeling the fate of DMS oxidation products, including heterogeneous aerosol processes and their interaction with clouds.

2. Model Description

We only give a brief overview of the model. A detailed description of a comparable 1-D boundary layer model is given by *Ackerman et al.* [1995], and a more general overview on boundary modeling is given by *Stull* [1988]. The underlying dynamical model applied here is the nonhydrostatic mesoscale meteorological model, Méso-NH, of Laboratoire d'Aérologie and Météo France [*Lafore et al.*, 1998], which is based on concepts of earlier models from both groups: the hydrostatic mesoscale model SALSA [*Nickerson et al.*, 1986] and the former French meteorological forecast model PERIDOT. Note in particular that SALSA's boundary layer parameterizations have been validated in dedicated international model intercomparisons [*Bechtold et al.*, 1996; *Bretherton et al.*, 1998]. Meso-NH is used here in its 1-D configuration (see also *Mari et al.* [this issue] for a 3-D mesoscale simulation of DMS in LB with the same model).

The prognostic variables are the vertical profiles of latitudinal and longitudinal wind components (u, v), potential temperature (Θ), water vapor (q_v), cloud (q_c), and rain (q_r) water mixing ratios, the mixing ratios of the different chemical species (c_i) and turbulent kinetic energy $(\bar{e})$. Note that $\bar{e}$ is a second-order quantity, defined as $\bar{e} = 0.5(\overline{u'u'} + \overline{v'v'} + \overline{w'w'})$, where u', v', and w' are the turbulent fluctuations around the averages of the three wind speed components and overbars denote Reynolds averaging [*Stull*, 1988]. The basic equations implemented in the model in its 1-D configuration are

$$\frac{\partial u}{\partial t} = \frac{\partial}{\partial z}\left(K_m \frac{\partial u}{\partial z}\right) - w_{ls}\frac{\partial u}{\partial z} + f(v - v_g) \quad (1)$$

$$\frac{\partial v}{\partial t} = \frac{\partial}{\partial z}\left(K_m \frac{\partial v}{\partial z}\right) - w_{ls}\frac{\partial v}{\partial z} - f(u - u_g) \quad (2)$$

$$\frac{\partial \Theta}{\partial t} = \frac{\partial}{\partial z}\left(K_h \frac{\partial \Theta}{\partial z}\right) - w_{ls}\frac{\partial \Theta}{\partial z} + Q_\Theta^{\text{diab}} \quad (3)$$

$$\frac{\partial q_j}{\partial t} = \frac{\partial}{\partial z}\left(K_h \frac{\partial q_j}{\partial z}\right) - w_{ls}\frac{\partial q_j}{\partial z} + Q_{q_j}^{\text{diab}} ;$$
$$j \in \{v, c, r\} \quad (4)$$

$$\frac{\partial c_i}{\partial t} = \frac{\partial}{\partial z}\left(K_h \frac{\partial c_i}{\partial z}\right) - w_{ls}\frac{\partial c_i}{\partial z} + Q_{c_i}^{\text{chem}} \quad (5)$$

$$\frac{\partial \bar{e}}{\partial t} = \frac{\partial}{\partial z}\left(K_m \frac{\partial \bar{e}}{\partial z}\right) - w_{ls}\frac{\partial \bar{e}}{\partial z}$$
$$+ K_m \left[\left(\frac{\partial u}{\partial z}\right)^2 + \left(\frac{\partial v}{\partial z}\right)^2\right]$$
$$+ K_h \frac{g}{\Theta}\frac{\partial \Theta}{\partial z} - \epsilon . \quad (6)$$

where f is the Coriolis parameter and u_g and v_g are the components of the geostrophic wind. The parameter w_{ls} is the synoptic-scale vertical velocity, and K_m and K_h are the turbulent mixing coefficients for momentum and heat, respectively. Q_Θ^{diab} and $Q_{q_i}^{\text{diab}}$ are the diabatic terms in the heat and humidity equations, and $Q_{c_i}^{\text{chem}}$ is the photochemical production and loss term for species i. The parameter g is the gravitational constant, and ϵ is the dissipation rate of turbulent kinetic energy.

All model variables are represented on a semistaggered grid with 60 vertical levels, which means that turbulent fluxes are defined midway between the grid points where the scalar variables are located in order to increase numerical precision [*Haltiner and Williams*, 1980]. The vertical resolution is 20 m between the surface and 500 m altitude, the lowest model level being located at 10 m. Above 500 m, the vertical grid spacing increases continously up to the model's top at 3200 m (e.g., the grid spacing is 60 m at 1000 m and 200 m at the top). The time step is 50 s, using a Leapfrog-type time discretization for dynamics and a time splitting technique for chemistry. The turbulent mixing coefficients are proportional to $L\sqrt{\bar{e}}$, where the mixing length L is calculated nonlocally as a function of stability [*Bougeault and Lacarrère*, 1989]. The dissipation term ϵ is set proportional to $\bar{e}^{3/2}/L$ [*Redelsperger and Sommeria*, 1981]. In order to calculate the diabatic terms due to radiative heating (Q_Θ^{diab}) and phase changes in the water variables $(Q_{q_i}^{\text{diab}})$, the following parameterizations are used: a fractional cloudiness scheme [*Bechtold et al.*, 1992], shortwave and infrared radiation [*Morcrette*, 1989], and a bulk microphysical scheme [*Kessler*, 1969]. Surface momentum, heat, and humidity fluxes are parameterized following *Charnock* [1955] and enter the system as surface boundary conditions. Time dependant synoptic-scale forcings for the horizontal pressure gradient are imposed as a geostrophic wind (u_g, v_g), and synoptic-scale divergence is accounted for by prescribing a vertical velocity (w_{ls}). What makes our 1-D column model a Lagrangian model is the fact the geostrophic wind, the synoptic-scale vertical velocity, and the sea surface temperature (SST) are varied following the trajectory of LB. All those forcing terms are extracted from the European Centre for Medium-Range Weather Forecasts (ECMWF) meteorological analyses at the locations indicated in Figure 1. The synoptic-scale vertical velocity w_{ls} is obtained by vertical integration of the analyzed horizontal wind divergence. The SST used in the model has been increased by 1 K relative to the analyzed SST, based on the fact that the R/V *Discoverer* SST in situ measurements suggest such
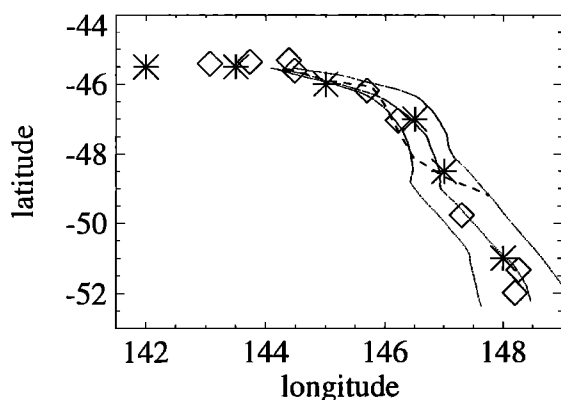
Figure 1. ACE 1 Lagrangian B: position of balloons (fine dotted lines, from left to right: balloons 6, 0, and 8), lowest points in aircraft soundings (diamonds), location for which forcing terms have been extracted from the ECMWF analyses (stars, every 6 hours, starting on December 7, 1800 UTC), and trajectory of the R/V *Discoverer* (dashed line, December 9, 0000-2000 UTC).

a bias. It turns out that the model is very sensitive to small variations in SST, as will be discussed later.

The chemical part of the model is an improved version of the one described by *Suhre and Rosset* [1994a] and *Suhre et al.* [1995]. The reaction scheme selected for the chemical module includes 50 gas phase reactions for 23 prognostic chemical species (see appendix). No aqueous phase chemistry is treated. The chemical solver for the resulting stiff differential equations is a linearized semi-implicit method [*Ramaroson et al.*, 1992; *Suhre and Rosset*, 1994b]. All reaction rates are temperature and pressure dependant [*DeMore et al.*, 1992]. Photolysis rates are updated every 15 min using a two-stream radiative transfer model [*Petropavlovskikh*, 1995; *Madronich and Weller*, 1990; *Toon et al.*, 1989]. Modeled clouds are taken explicitly into account in the radiative transfer calculation at the vertical resolution of the model. Cloud optical properties (optical thickness and effective radius) are parameterized following *Fouquart et al.* [1990], based on the cloud water mixing ratio at each model level. DMS sea-air fluxes are parameterized either after *Wanninkhof* [1992] (W92 hereafter) or after *Liss and Merlivat* [1986] (LM86 hereafter), accounting for changes in seawater temperature and modeled surface wind speed. The Schmidt number dependance for the Liss and Merlivat exchange velocity is implemented as described by *Gabric et al.* [1995]. DMS concentrations in seawater have been interpolated onto the Lagrangian trajectory based on measurements made on the R/V *Discoverer* [*Bates et al.*, this issue (b)]. Dry deposition velocities are imposed for the soluble species (SO_2, H_2O_2, CH_3OOH, HNO_3) based on the aerodynamic resistance calculated by the model, assuming a laminar resistance of 0.2 s/cm and neglectable surface resistance [*Baer and Nester*, 1992]. For ozone, a surface resistance of 20 s/cm is assumed, which is in agreement with turbulent ozone fluxes measured near

the surface on the National Center for Atmospheric Research (NCAR)/C130 [*Wang and Linlin*, 1997; Q. Wang et al., unpublished manuscripts, 1998a, b]. No wet deposition is treated as the clouds observed in LB were mostly nonprecipitating.

Potential temperature and humidity are initialized using the first NCAR/C130 aircraft sounding on flight 24 (24A on December 7, 1995, 2120 UTC, compare Table 1). The initial wind is set equal to the geostrophic wind, which agrees with the wind observed in sounding 24A. Initial profiles for O_3, H_2O_2, CH_3OOH, DMS, and CH_3I are also taken from sounding 24A. All radical concentrations are initially set to zero. The following species are initialized assuming vertically homogeneous mixing ratio profiles based on different observations made on the NCAR/C130 and the R/V *Discoverer*: 10 ppt NO_x (J. Bradshaw, unpublished data, 1996; T. Carsey et al., unpublished manuscript, 1998), 350 ppt HNO_3 (T. Carsey et al., unpublished manuscript, 1998) (assuming $HNO_3 = NO_y - NO_x$), 65 ppb CO [*Kok et al.*, this issue], 1.69 ppm CH_4 (Blake et al., unpublished manuscript, 1998), 35 ppt SO_2 (A. R. Bandy et al., unpublished manuscript, 1998). HCHO has not been measured and is initialized to 160 ppt, based on box model calculations. The total simulation time is 28.5 hours, covering the LB experiment until the last aircraft sounding (26C) on December 9, 1995, 0147 UTC.

3. Results and Discussion

The results of the 1-D Lagrangian simulations will be presented as direct comparisons between the nine aircraft soundings made during flights 24-26 and vertical profiles calculated by the model at the same time, that is, potential temperature, water vapor mixing ratio, cloud water mixing ratio, wind speed and direction, turbulent kinetic energy, O_3, OH, H_2O_2, CH_3OOH, DMS, and CH_3I (Figures 2-13). NO and CO profiles

Table 1. Time of the Nine NCAR/C130 Aircraft Soundings Used in This Study: Four From Flight 24, Two From Flight 25, and Three From Flight 26.

| ID[a]	Date	Time, UTC
Flight 24		
24A	Dec. 7	2120
24X	Dec. 8	0027
24Y	Dec. 8	0227
24B	Dec. 8	0341
Flight 25		
25A	Dec. 8	0858
25B	Dec. 8	1310
Flight 26		
26A	Dec. 8	2113
26B	Dec. 9	0015
26C	Dec. 9	0147

[a]The identifiers of each sounding are reproduced above the different profiles presented in Figures 2-13.
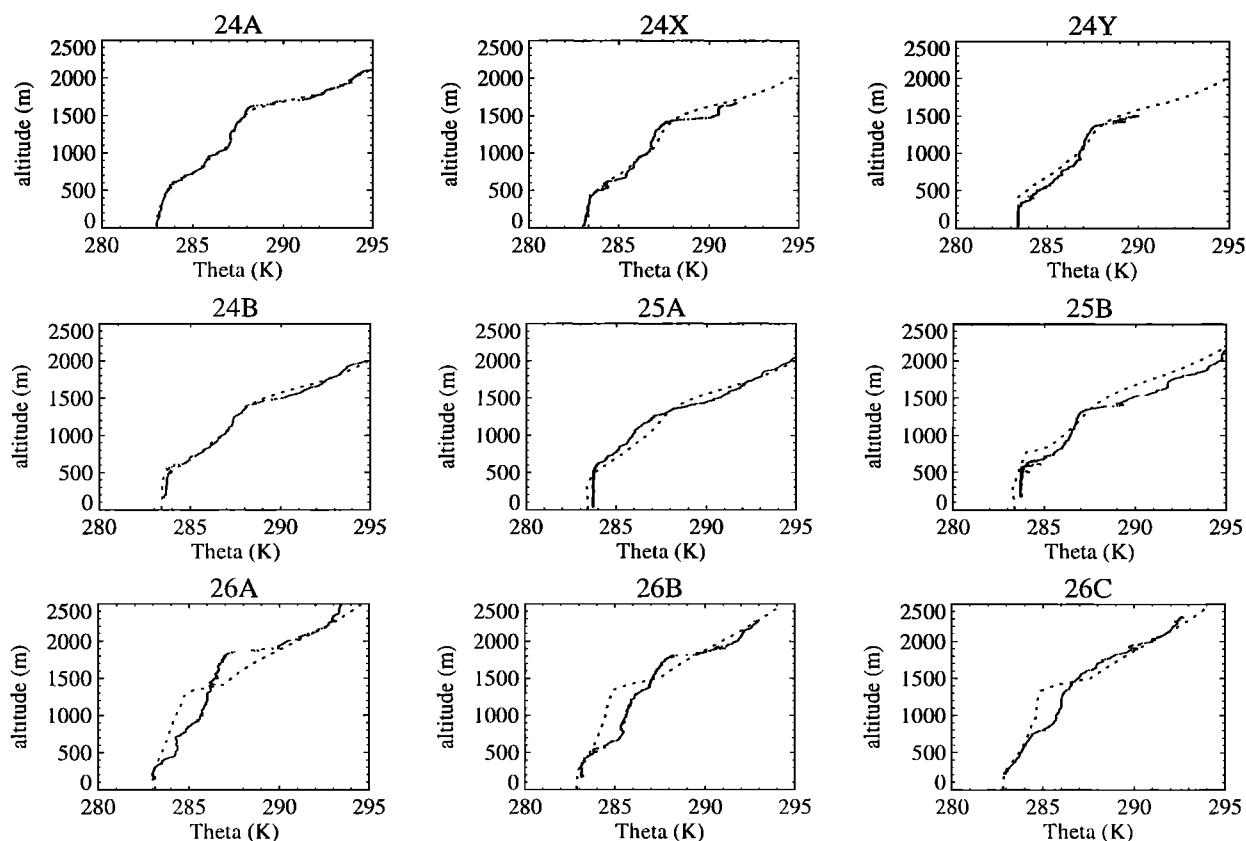
Figure 2. Potential temperature: data (fine dots), and simulation (dotted line). The identifiers of each sounding (e.g., 24A) are explained in Table 1. All soundings are displayed in temporal order from left to right and then from top to bottom.
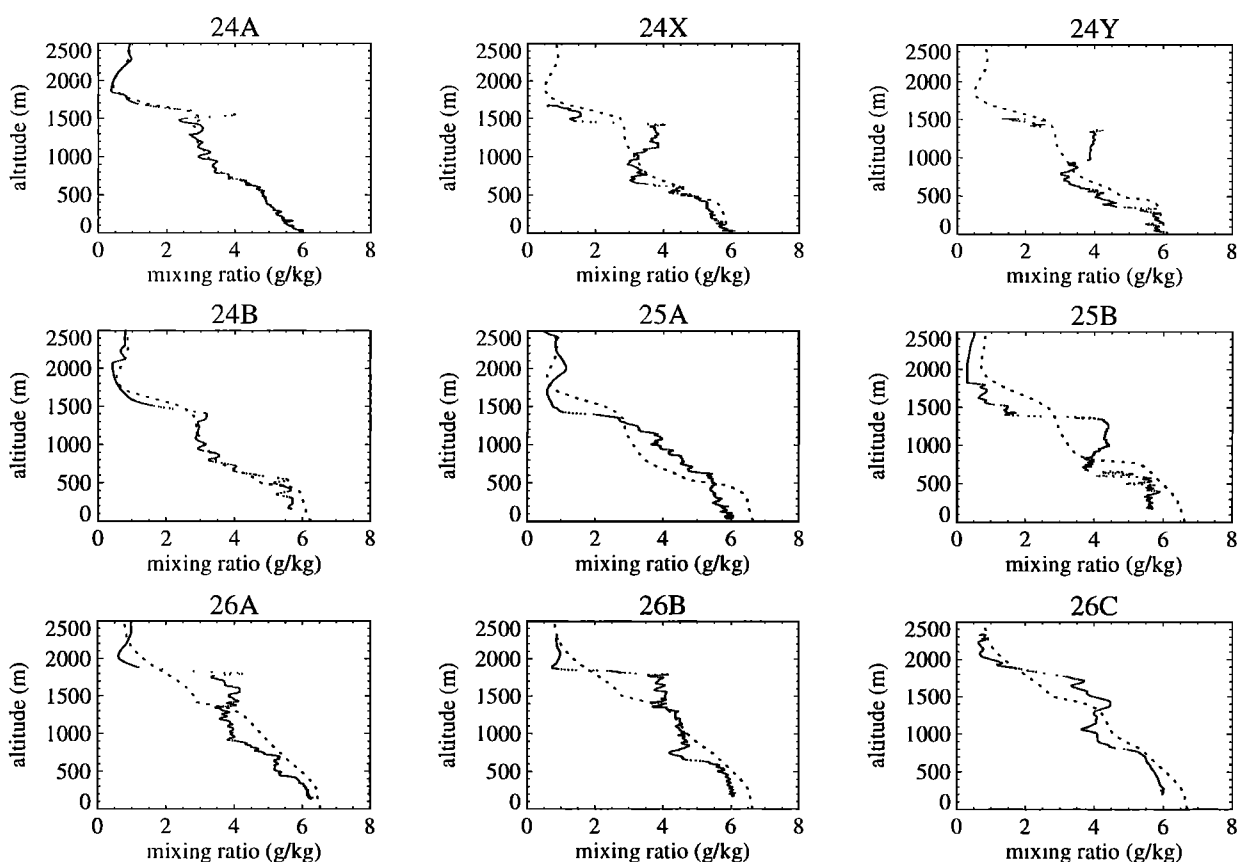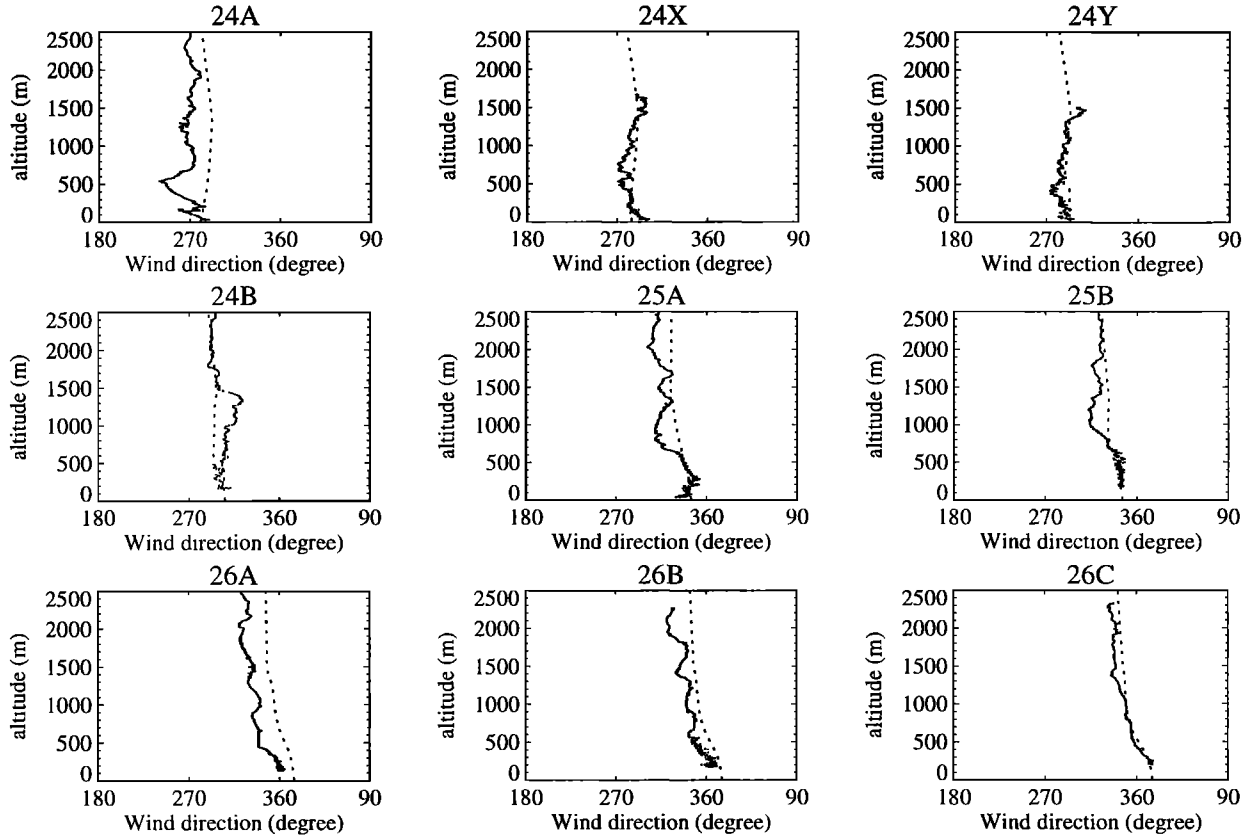

Figure 3. Water vapor mixing ratio: data (fine dots), and simulation (dotted line).
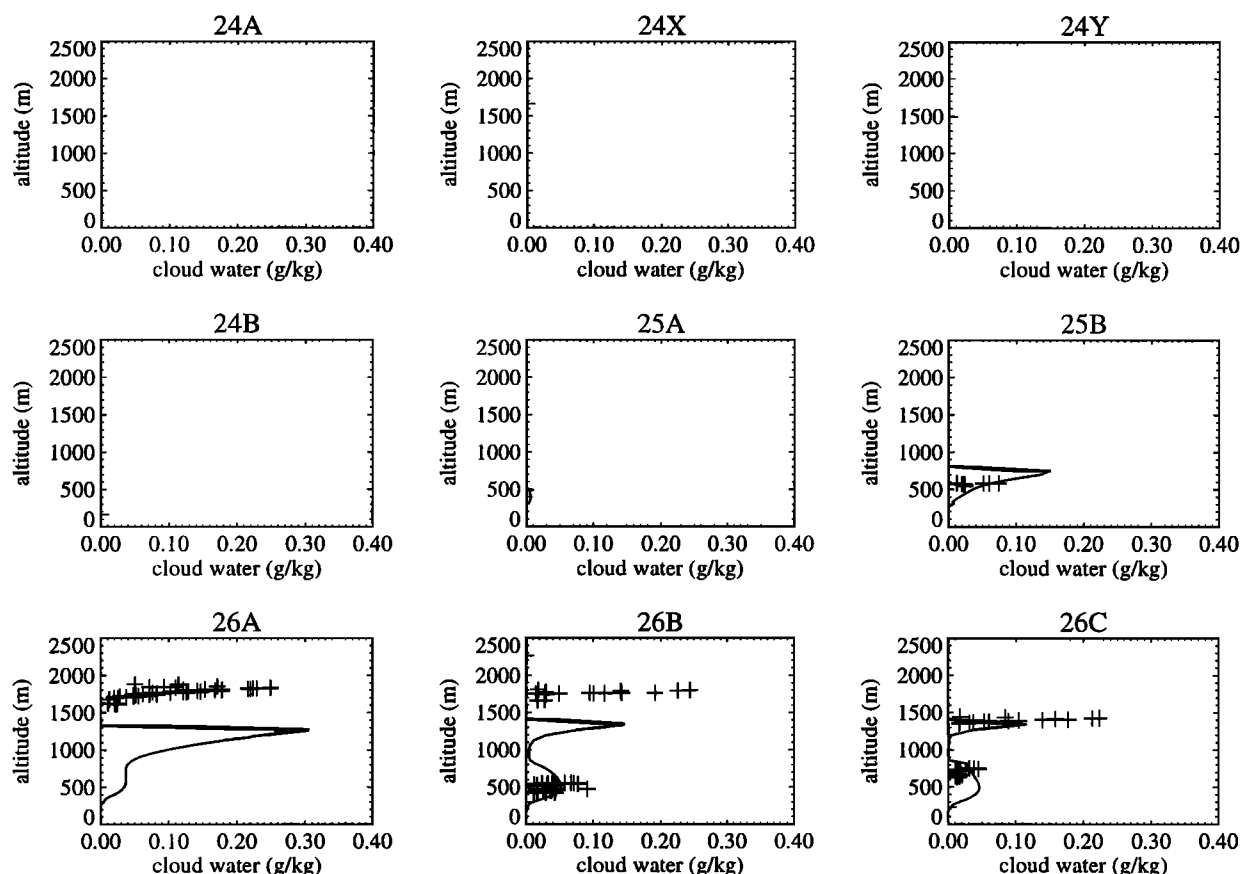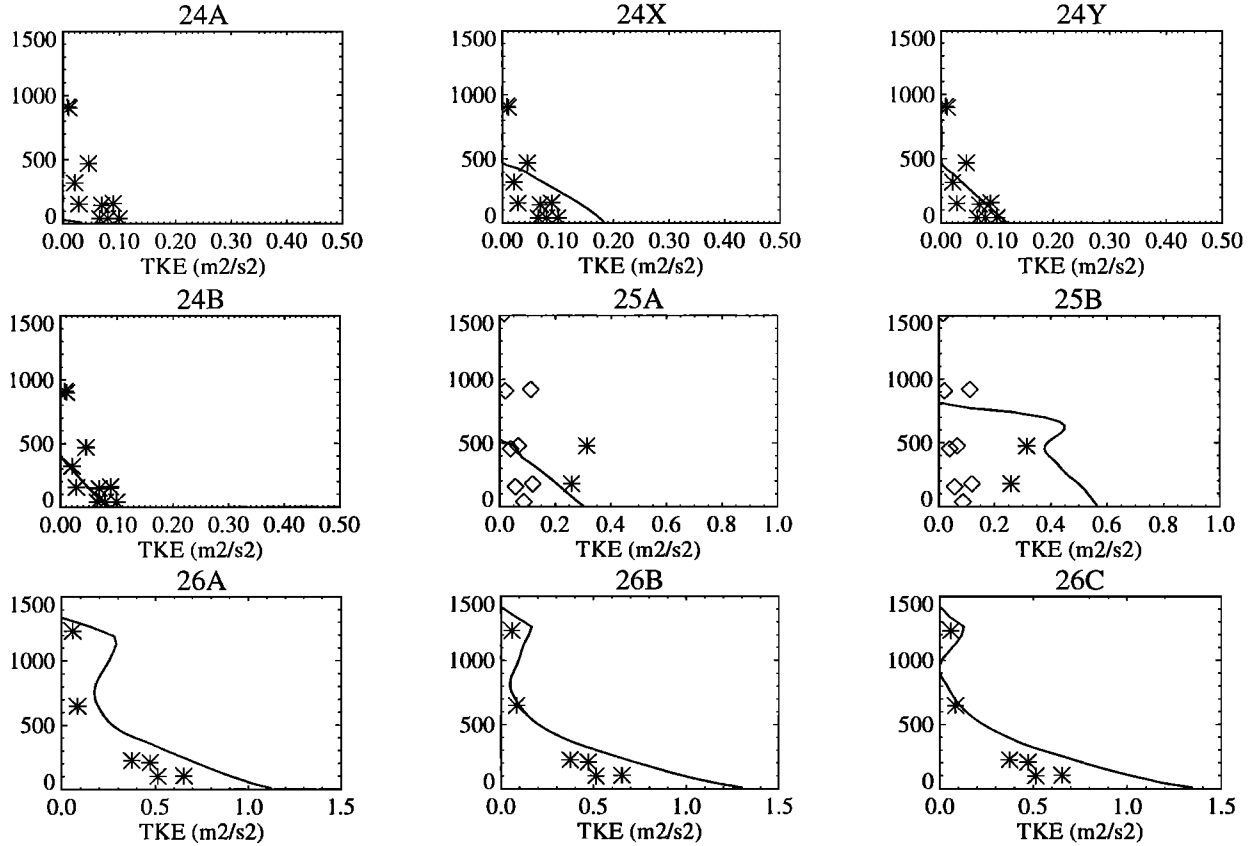
Figure 4. Cloud water mixing ratio: data (crosses), and simulation (solid line). Note that the observations are biased by the fact that the aircraft tried to avoid clouds as much as possible.
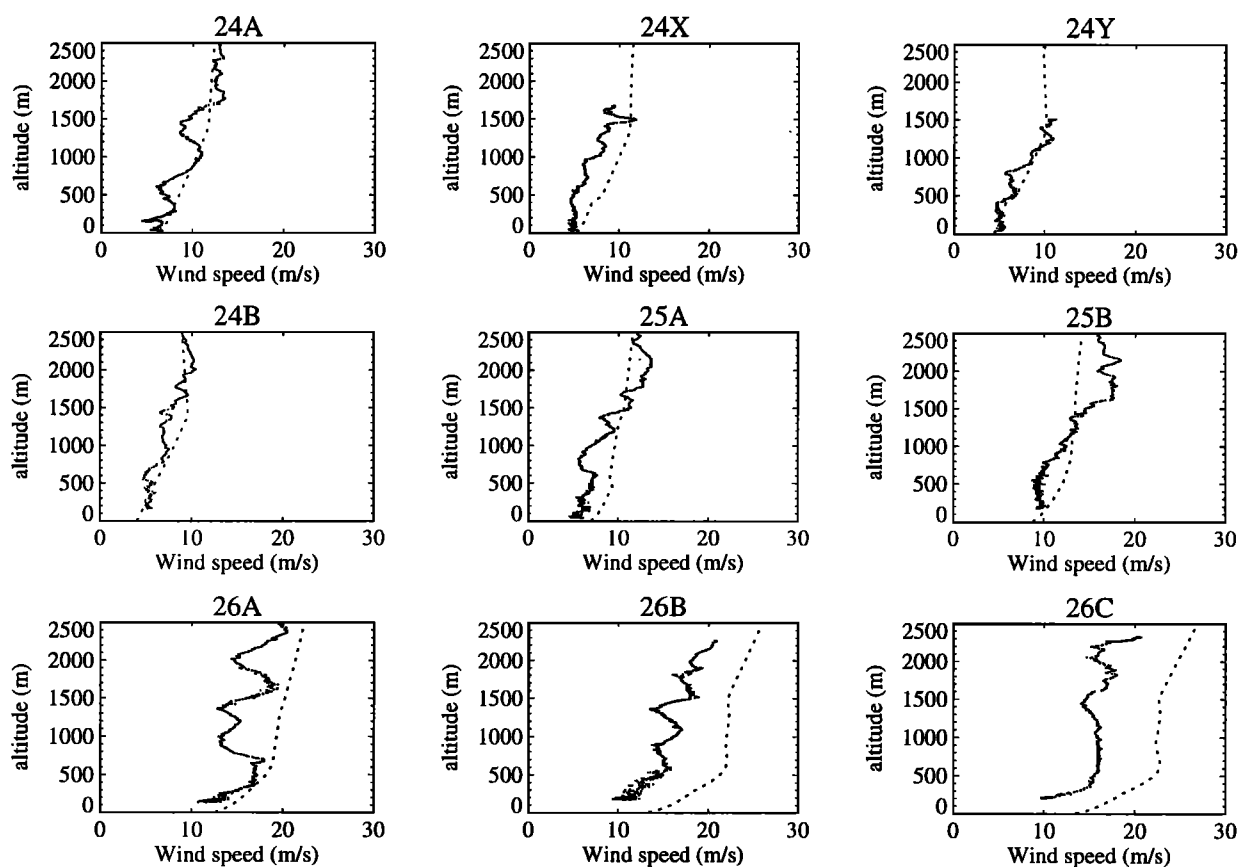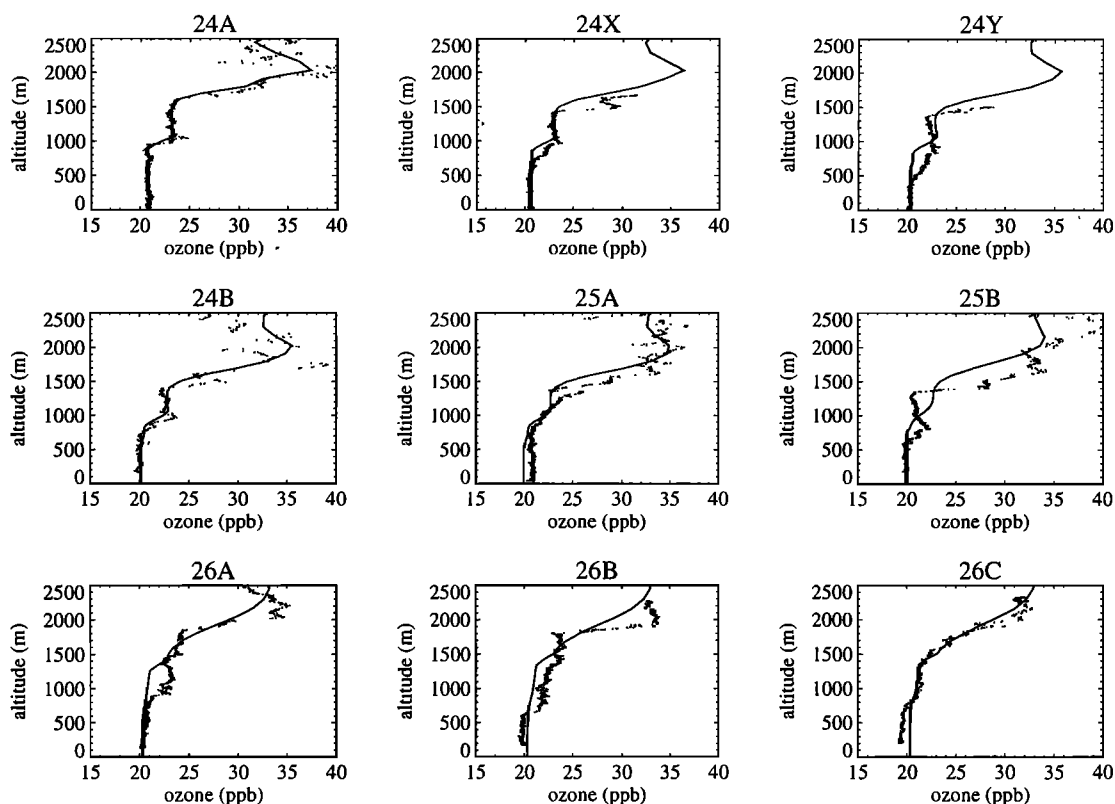
Figure 5. Wind speed: data (fine dots), and simulation (dotted line).

Figure 6. Wind direction: data (fine dots), and simulation (dotted line).

Figure 7. Turbulent kinetic energy, $\bar{e} = 0.5(\overline{u'u'} + \overline{v'v'} + \overline{w'w'})$: data (stars, diamonds), and simulation (solid line). Observed TKE is derived from 20 Hz measurements of wind speed. As flight 25 took place over a zone with a strong gradient in sea surface temperature, TKE measurements are discriminated into TKE observed over warmer water (stars) and over colder water (diamonds, refer to Q. Wang et al., unpublished manuscript, 1998a, b, for details). Note the different scaling for the three flights and the limitation of the plots to 1500 m altitude.

Figure 8. Ozone mixing ratio: data (fine dots), and simulation (solid line). Detection limit is 0.2 ppb: the measurement error is set to a relatively high value of 10%, due to oil that got blown back into the UV instrument.
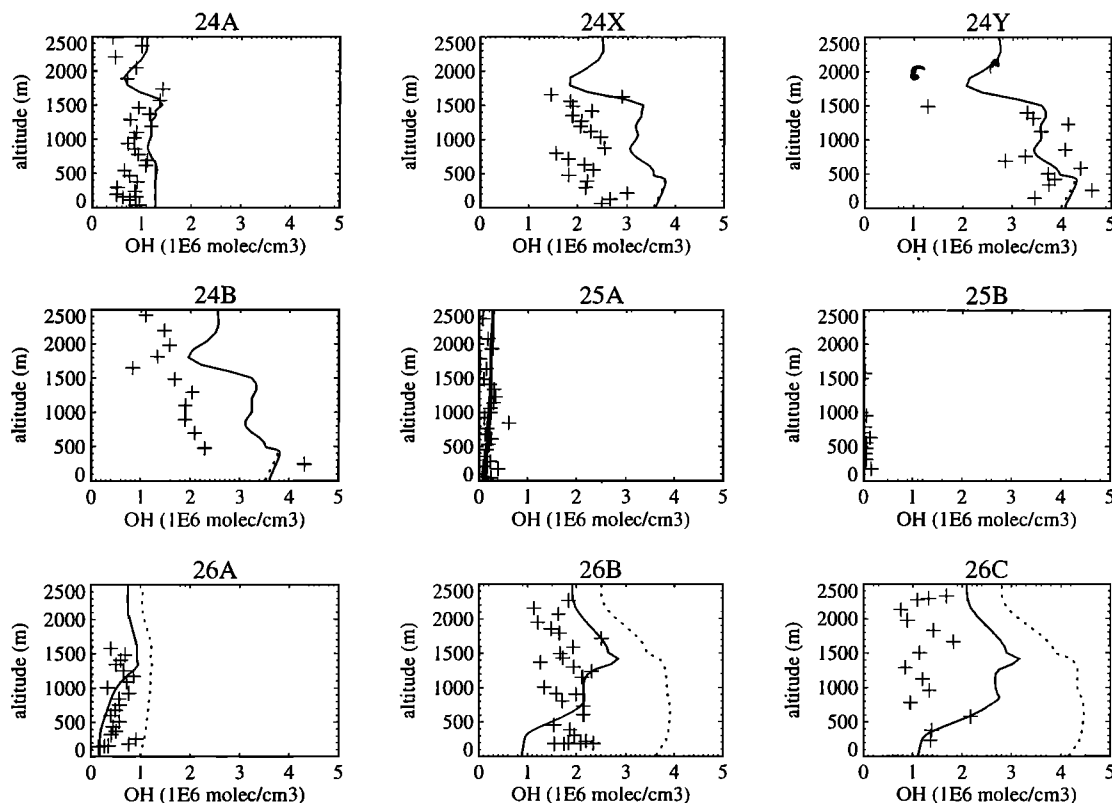
Figure 9. Hydroxyl radical concentration: data (crosses), and simulation including clouds in the calculation of photolysis rates (solid line), simulation assuming clear-sky conditions (dashed line). Two-sigma error limits in the boundary layer are ±42%.
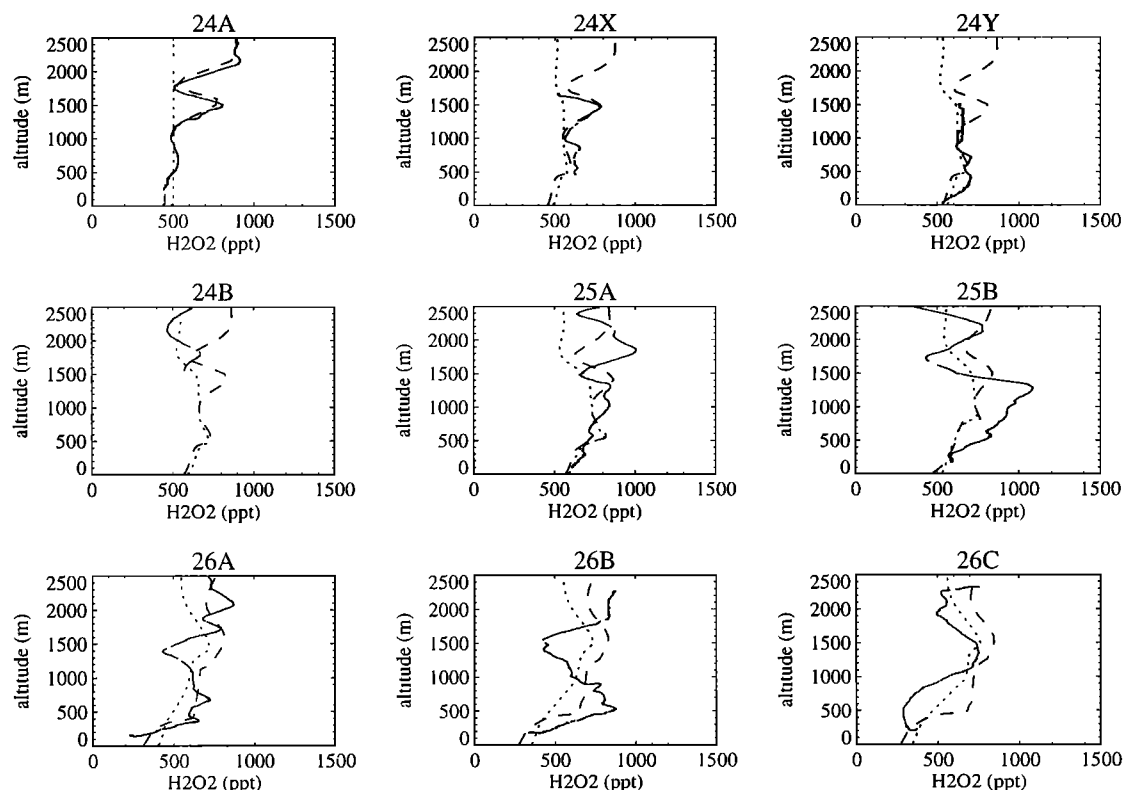
Figure 10. Hydrogen peroxide (H_2O_2) mixing ratio: data (fine dots), simulation with vertically constant initial profile (dotted line), and simulation with observed initial profile and SST lowered by 3 K after 15 hours of simulation (dashed line). The detection limit is 40 pptv, and the uncertainty is 15%.
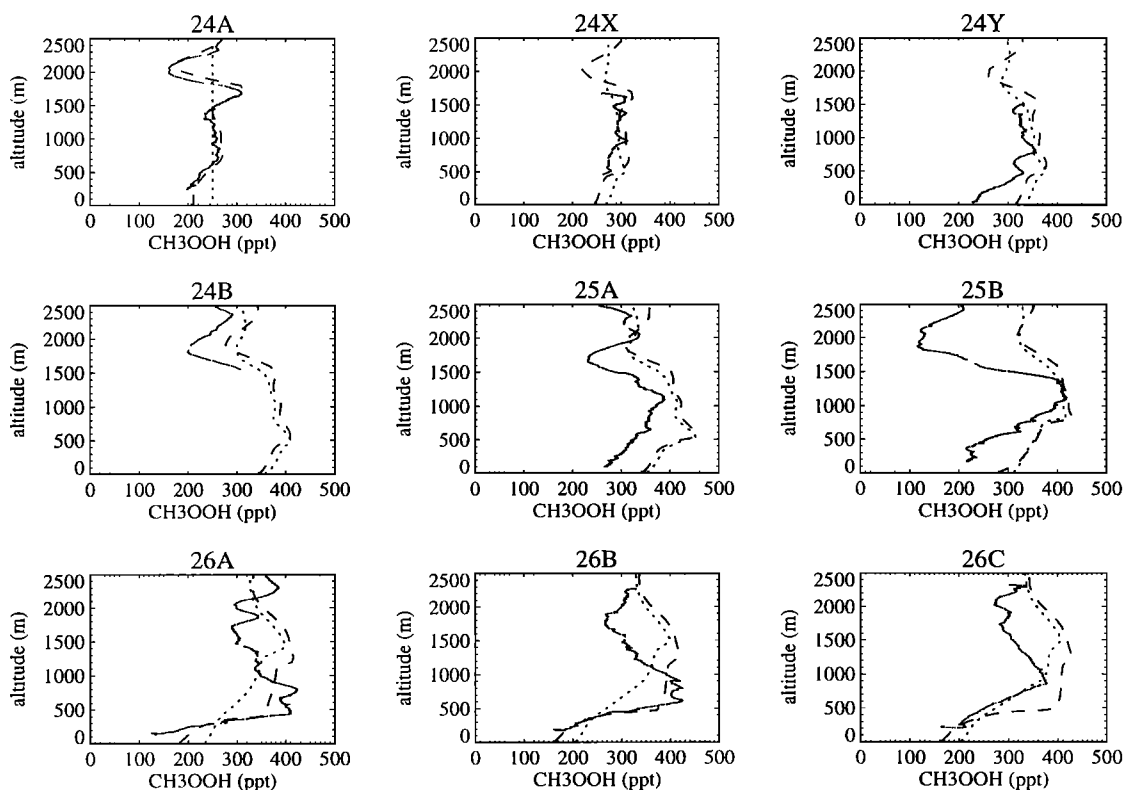
Figure 11. Methylhydroperoxide (CH_3OOH) mixing ratio: data (fine dots), simulation with vertically constant initial profile (dotted line), and simulation with observed initial profile and SST lowered by 3 K after 15 hours of simulation (dashed line). The detection limit is 60 pptv, and the uncertainty is 25%.

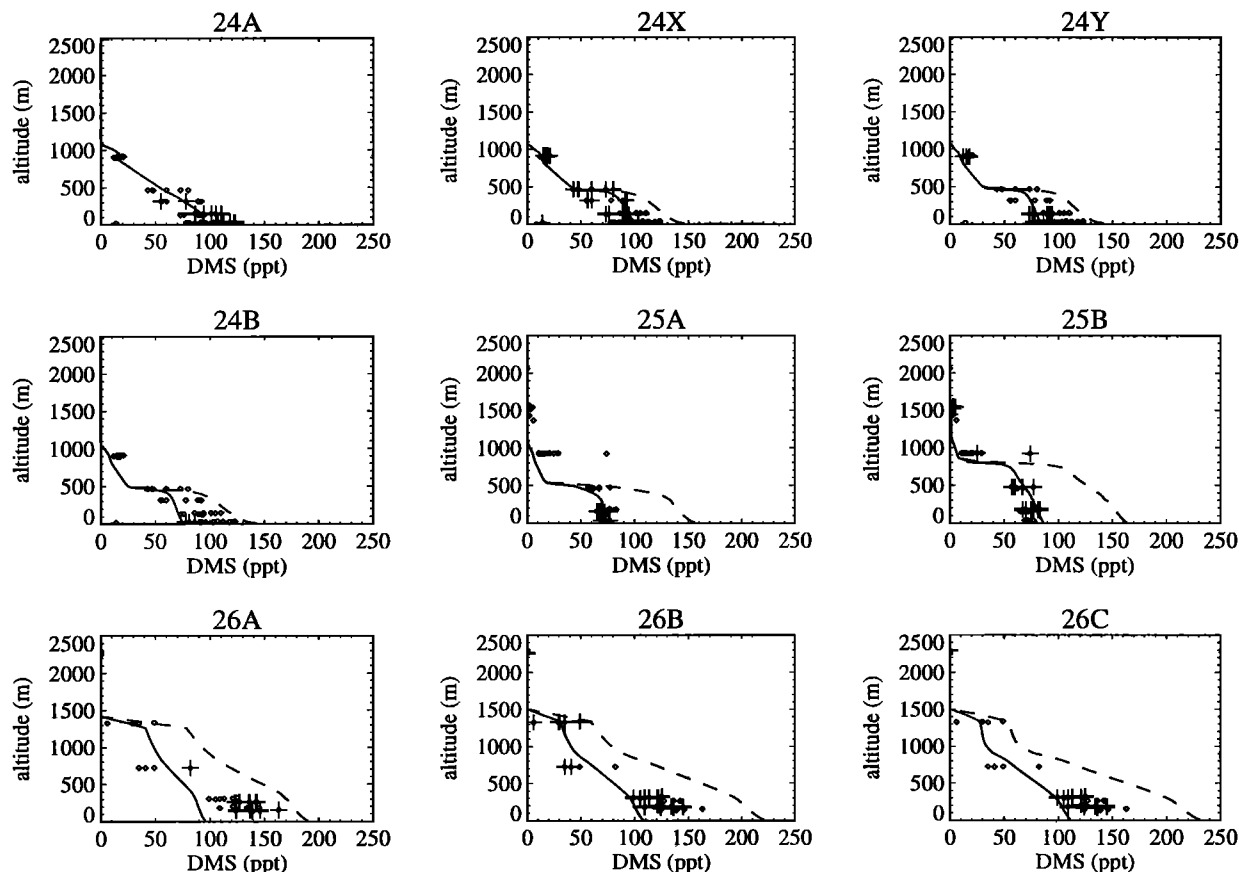**Figure 12.** Dimethyl sulfide (DMS) mixing ratio: no DMS observations were made during aircraft soundings, measurements made during horizontal circles that are closer than 1.5 hours to aircraft sounding are presented by crosses, and other data from the same flight are indicated by dots. Simulation with *Liss and Merlivat* [1986] DMS flux parameterization (solid line), and simulation with *Wanninkhof* [1992] DMS flux parameterization (dashed line) were made using the same initial DMS profile (24A). The detection limit for DMS measurements on flights out of Tasmania is 2 ppt, and precision is 1 ppt.

have also been measured, but for both data sets the noise-to-signal ratio is too large to allow a meaningful comparision with the model. All soundings are identified by their respective flight number and a letter as described in Table 1. Flights 24 and 26 were daytime flights: flight 25 took place at night. Universal time (UTC) is used throughout the discussion, local Australian Eastern Standard Time (AEST) being AEST equal to UTC + 10 hours. The goal of the first part of this section is to present the general dynamical setting and to show that the dynamical part of our 1-D simulation is able to represent the MBL as it was observed in LB. The remaining parts present the chemical simulations made in this dynamical framework and discuss the results.

3.1. Dynamics

The observed boundary layer during LB was characterized by a distinct two-layer structure, as can be seen in the profiles of potential temperature (Figure 2), humidity (Figure 3), ozone (Figure 8), peroxides (Fig-

ures 10 and 11), and to a lesser extent in the DMS (Figure 12) and CH_3I (Figure 13) data. The upper layer, located between roughly 500 m and the main inversion, was stably stratified and nearly nonturbulent. Turbulence in the lower layer was very weak during flight 24. During flight 25, some turbulence was generated by buoyancy and wind shear, whereas flight 26 encountered a stable, purely shear driven boundary layer with stronger turbulence in the lowest layer (Figure 7, see also Q. Wang et al., unpublished manuscripts, 1998a, b). At the onset of LB, light westerly winds prevailed under a cloud free sky. The wind accelerated during the night and turned to northerly flow (Figures 5 and 6). The SST beneath the air column decreased as the column was advected southward from Subantarctic over polar water [*Bates et al.*, this issue (a)], resulting in a cooling of the lowest atmospheric layer. Clouds developed during the night, and flight 26 took place under cloudy conditions (Figure 4). Two cloud layers developed in the MBL, one topping the lower layer, and a second in the upper layer. Cloud formation in the lowest layer is due to cooling of the air mass as it moves
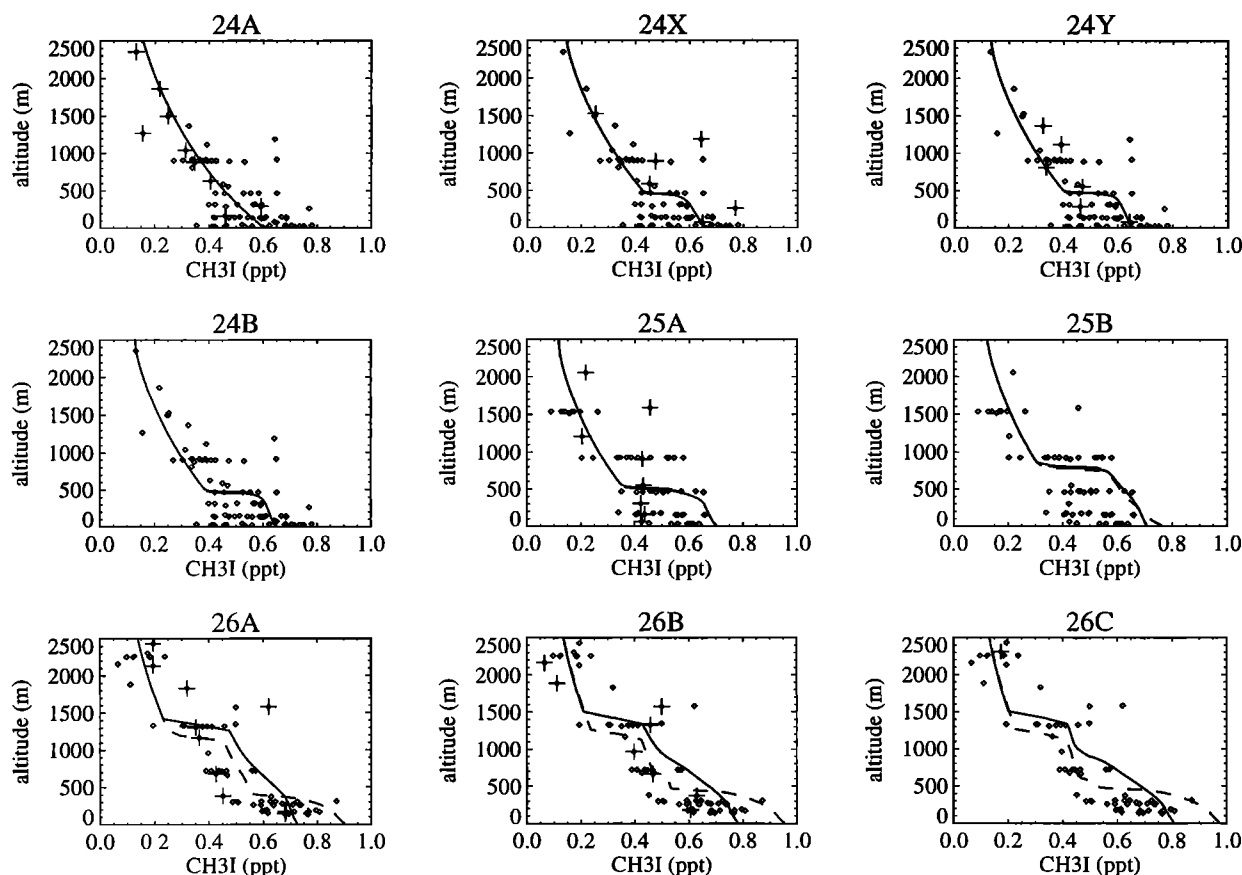
Figure 13. Methyl iodine (CH_3I) mixing ratio: data on aircraft soundings (crosses), other data on each flight (dots), simulation using a CH_3I flux equal to the *Liss and Merlivat* [1986] DMS flux scaled by 250, which corresponds to the ratio between the observed DMS and CH_3I mixing ratios near the surface (solid line), and simulation with SST lowered by 3 K after 15 hours of simulation (dashed line). The limit of detection for CH_3I measurements is 0.03 ppt, precision is 5%, and accuracy is ±20%.

over the colder ocean. Cloud formation in the upper layer is attributed to cooling by lifting in synoptic-scale convergence and to a drop in atmospheric surface pressure. Note also that a layer of altostratus clouds was observed by the NCAR/C130 at the beginning of flight 26 on its descent from cruise altitude to the balloons and again during its climb out to Hobart at the end of that flight. These clouds are visible on GMS infrared satellite images and on some of the SABL lidar observations. The altostratus layer, which was located above the model domain, has been taken into account in the calculation of photolysis rates.

According to the meteorological analyses from ECMWF, surface pressure dropped from 1012 hPa on December 7 1800 UTC to 997 hPa on December 9 0000 UTC, following the path of the Lagrangian trajectory. Analyzed SST below the Lagrangian air column decreased from 283.8 to 281.3 K in the same period. Note that radiometric measurements of SST aboard of the NCAR/C130 were in general about 1-3 K lower than the ECMWF analyses. SST measured in situ on the R/V *Discoverer* in the launch region of

the balloons (144.5° E, 45.5° S), in contrast, was about 1 K higher than the ECMWF analyzed SST. In addition, ECMWF analyses show that the synoptic-scale flow was divergent in the beginning of LB, followed by significant synoptic-scale convergence, in particular on December 8 1200 UTC (Figure 14b). This convergence is confirmed in the ECMWF analyses of potential temperature and humidity (see Q. Wang et al., unpublished manuscript, 1998a), and agrees with the observations made during the nine aircraft soundings (e.g., upward movement of the 295 K isentrope between sounding 25B and 26A (Figure 2)). Note that there is in general good agreement between the ECMWF analyses of temperature and humidity and the NCAR/C130 aircraft soundings (presented in Q. Wang et al., unpublished manuscript, 1998b). This is also true for the analyzed wind speed and direction, which follow the observed rotation in wind direction and acceleration of wind speed during flight 25. However, the analyzed wind speed during flight 26 is overestimated by about 3-4 m/s as compared to the NCAR/C130 soundings. Meteorological balloon soundings, made on a regular basis on the
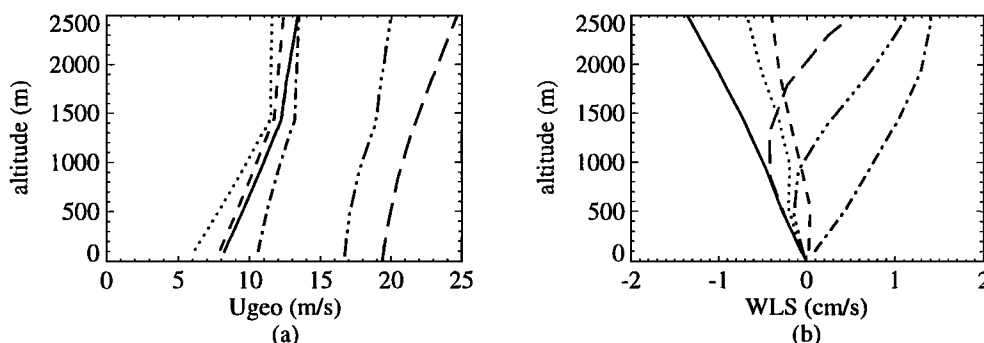
Figure 14. (left) Geostrophic wind speed and (right) synoptic-scale vertical velocity, derived from ECMWF meteorological analyses following the trajectory of LB, as indicated in Figure 1 (negative vertical velocity corresponds to subsidence); temporal order is: December 7 1800 UTC (solid lines), December 8 0000 UTC (dotted lines), 0600 (dashed lines), 1200 (dash-dotted lines), 1800 (dash-triple-dotted lines), and December 9 0000 UTC (long-dashed lines).

R/V _Discoverer_, have been assimilated into ECMWF analyses and are certainly one of the reasons for their general good agreement with the aircraft observations.

We now show that the 1-D Lagrangian model, forced with ECMWF-analyzed geostrophic wind (Figure 14a), divergence (Figure 14b), and SST (increased by 1 K) and initialized with potential temperature and water vapor mixing ratio from the first NCAR/C130 aircraft sounding (24A), is able to represent the dynamical structure of the marine boundary as observed during Lagrangian flights 24 and 25. Deviations between the model and the observations that occured after 24 hours of simulation on flight 26 are discussed.

Wind direction is modeled with a better than ±15° accuracy over the entire LB experiment (Figure 6). Modeled horizontal wind speed agrees with observations until sounding 26A. At the end of LB (sounding 26C), it is overestimated by about 6 m/s (Figure 5). This is attributed to two factors: (1) the ECMWF analysis overestimates the observed wind speed by 3-4 m/s, and (2) a 1-D model admits undamped inertial oscillations, that are excited when the geostrophic wind forcing is time dependant [_Stull_, 1988]. This results in a rotation of the actual wind vector around the geostrophic wind vector, thus allowing for supergeostrophic wind speeds.

Potential temperature evolution in the free troposphere is reproduced for the entire LB experiment, the difference between the modeled and observed 290 K isentrope height being always smaller than 100 m (Figure 2). A simulation excluding synoptic-scale vertical transport gave very different results and disagreed with the observations. The height of the 295 K potential temperature level at the end of the simulation was underestimated by 500 m in this case. During LB, synoptic-scale vertical transport is the dominant term in the evolution of potential temperature in the free troposphere, since radiative heating and cooling can be shown to be of minor importance on this timescale, turbulent and advective transport of heat has not to be accounted for, and no latent heat exchange with the

cloud phase takes place at this altitude. Therefore the agreement between the observed and modeled potential temperature in the free troposphere validates the synoptic-scale vertical velocity used in this study.

Potential temperature in the MBL during flights 24 and 25, and in particular the height of the main MBL inversion as well as the height of the separation between the lower and the upper layer, are modeled with a precision better than 100 m. During flight 26, the MBL vertical structure became more complex. Because of a decreasing SST at the end of LB, a cold layer developed in the lower layer. The 1-D model fails to "see" this lowest layer and erroneously mixes the entire MBL through. As this leads to a cooling of the upper layer, the main inversion in the model is lower than in the observations (in particular, in soundings 26A and 26B). Lidar observations show that the horizontal structure of the MBL became relatively heterogeneous on a small scale, with numerous small cumulus clouds developing in the upper layer. This fine scale structure could not be reproduced by our 1-D model, despite its fractional cloudiness parameterization. More sophisticated cloud and turbulence parameterizations might improve the simulations (e.g., higher-order turbulent closure and a shallow convection scheme) but are beyond the scope of this work. However, a sensitivity test made by decreasing the SST by 3 K after 15 hours of simulation (after sounding 25B) actually generated a cold layer near the surface, showing the strong sensitivity of the simulation to SST forcing [see also _Wang and Linlin_, 1997; Q. Wang et al., unpublished manuscript, 1998b]. Note that there was up to 3 K difference between the NCAR/C130 and the R/V _Discoverer_ measurements. Thus part of the discrepancy between model and observations on flight 26 may be accounted for by uncertainties in the SST forcing. As can be seen in Figure 15, the overall profile of potential temperature of this "SST-3 K" simulation does not correspond to what was observed during LB. However, as this simulation captures the lowermost cold layer, not represented in the reference simulation, we will dis-
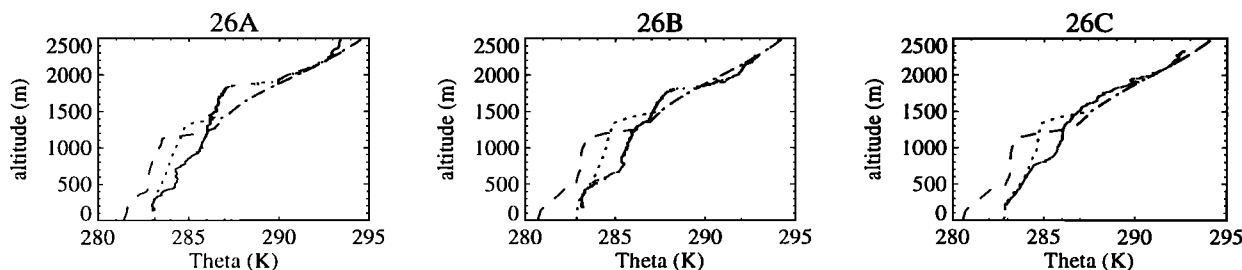
Figure 15. Potential temperature on flight 26: data as in Figure 2, and reference simulation (dotted line), with SST lowered by 3 K after 15 hours of simulation (dashed line).

cuss this case later with respect to those species that are most sensitive to surface exchanges, that is, DMS, hydrogen peroxides, and methylhydroperoxides.

The modeled water vapor mixing ratio profiles (Figure 3) capture the evolution of the overall two layer structure, but there is much more variability in the observations. For example, there is a considerable increase in observed water vapor between soundings 24A and 24X in the upper layer between 1000 m and 1500 m and a similar decrease between soundings 24Y and 24B. There is no physical mechanism that can induce such strong variations within such a small time span in a non-cloudy and mostly nonturbulent MBL in the absence of advective transport. Thus the difference between the different water vapor soundings has to be attributed to horizontal variability in the humidity field. During its different soundings, the aircraft obviously sampled slightly different air masses, more or less rich in water vapor. It is clear that a 1-D model cannot account for this kind of horizontal inhomogeneity. In sounding 26A and 26B, a three layer structure, as for potential temperature, can be observed in the water vapor data, but this structure is not reproduced by the model for the reasons discussed above.

The fact that flight 24 took place under clear-sky conditions as well as the onset of cloud formation during flight 25 are correctly modeled (Figure 4). During flight 26, cumulus clouds formed under the main inversion and in the lower layer. The altitude of the main inversion is too low in the model in soundings 26A and 26B, but clouds are predicted by the model in both layers in agreement with observations. The aircraft flight pattern was actually optimized in order to minimize encounter of clouds, due to constraints imposed by the aerosol measurement instruments that only operate in cloud free air. At the moment of sounding 26A, some clouds were also present in the lower layer but they were not sampled by the aircraft. The scattered cumulus clouds were in fact thicker than the aircraft soundings would suggest, so that the cloud water mixing ratios presented in Figure 4 are to be interpreted as a lower bound on the average liquid water profiles.

Turbulent kinetic energy ($\bar{e}$) is a key variable in boundary layer modeling as the turbulent vertical mixing of all dynamical and chemical variables is based on

an eddy diffusion coefficient that is proportional to $\sqrt{\bar{e}}$. Above the level where $\bar{e}$ falls to zero, no turbulent mixing takes place in the model. In that region, vertical transport is controlled by to the imposed synoptic-scale vertical velocity. As modeled $\bar{e}$ is a highly parameterized variable, it is more difficult to compare to measurements on an absolute scale. In addition, measurements of $\bar{e}$ require high-frequency observations of the three wind speed components over a horizontal distance that covers the largest turbulent length scales, typically several kilometers. Over that distance, $\bar{e}$ is assumed to be homogeneous and stationary, a condition that is not always satisfied (Q. Wang et al., unpublished manuscript, 1998a). As can be seen in Figure 7, the model "sees" the low turbulence on flight 24, its increase during flight 25, and highest values on flight 26, when wind speed and hence wind shear at the surface were strongest. Flight 25 took place over a region with large gradients in SST. Q. Wang et al. (unpublished manuscript, 1998b) show that for this flight stronger turbulence is correlated with flight sections over warmer water. The 1-D model cannot account for such fluctuations in SST, and as we chose to use a high SST forcing in the model, flight 25 should be compared to $\bar{e}$ measurements over high SST regions (represented by stars for flight 25 in Figure 7).

In conclusion, we can say that the 1-D Lagrangian model is able to reproduce the observed dynamical evolution of the MBL for flights 24 and 25. After 24 hours of simulation, the model tends to deviate from the observations as it fails to reproduce the more complex three layer structure observed on flight 26. This is partially due to inherent limitations of the 1-D approach that cannot account for horizontal variability in the developing cumulus clouds, but is also due to uncertainty in the SST forcing, as a sensitivity test with lowered SST shows. The evolution in the free troposphere, especially synoptic-scale vertical transport, is correctly modeled throughout the entire LB experiment, hence validating the synoptic-scale forcing of subsidence or ascent derived from ECMWF-analyzed wind divergence.

3.2. Chemistry: General Considerations

On the basis of the dynamical simulation discussed above, a number of simulations with coupled chemistry are performed. For the reference simulation, the
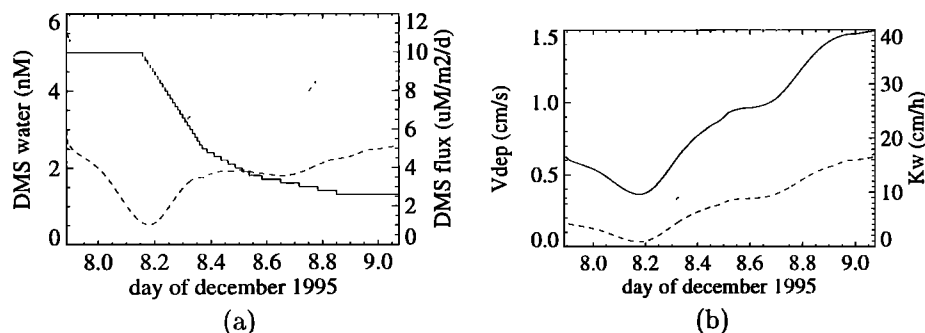
Figure 16. (left) DMS (water) from measurements on board of the R/V *Discoverer* and interpolated onto the Lagrangian trajectory as a function of time (solid line), and resulting DMS flux using *Liss and Merlivat* [1986] (dashed line) and *Wanninkhof* [1992] (dotted line) parameterizations. (right) Deposition velocity for soluble species (*V*dep, solid line), and exchange coefficient (*K*w) for DMS using *Liss and Merlivat* [1986] (dashed line) and *Wanninkhof* [1992] (dotted line) parameterizations.

DMS flux is calculated using the LM86 parameterization. In order to evaluate which DMS flux parameterization agrees best with the observations, a second simulation using W92 is made. A simulation assuming clear-sky conditions in the calculation of the photolysis rates is used to study the impact of clouds on photochemical OH production and a simulation where the SST is decreased by 3 K after 15 hours of simulation is used to look at the impact of the lowermost cold layer on flight 26, missed in the reference simulation.

Surface fluxes are imposed as lower boundary conditions to the turbulent flux term in the 1-D model. They depend in particular on wind speed at the lowest model level. The DMS flux also depends on the SST via the Schmidt number. DMS seawater concentrations are varied following the Lagrangian trajectory, using measurements from the R/V *Discoverer* [*Bates et al.*, this issue (b)]. The ship followed only part of the Lagrangian trajectory (Figure 1) and with a 24 hour delay. This delay is, however, smaller than the characteristic timescales for changes in seawater DMS concentrations and in SST. For flight 26, seawater DMS has been extrapolated. Figure 16a shows the imposed DMS seawater concentrations and the resulting DMS flux as a function of time; Figure 16b depicts the exchange velocity for DMS and the dry deposition velocity that are applied for the soluble species. Although DMS seawater concentrations were much higher in the beginning of LB (5 nM) than toward the end (1.3 nM), the resulting DMS flux was about as high in the beginning as it was in the end (about 5 $\mu M\,m^{-2}\,d^{-1}$ using LM86). This is due to the increase in wind speed during the experiment. The W92 parameterization yields a flux more than twice as high as that calculated with LM86. The dry deposition velocities of the soluble species vary between 0.7 cm/s in the beginning and 1.5 cm/s in the end. The corresponding friction velocity u_* varies between 0.15 m/s and 0.45 m/s and the roughness length z_0 between 0.01 and 0.3 mm. Both the modeled DMS flux and the modeled dry deposition velocity have a

minimum at about 0500 UTC on December 8 which is due to a minimum in modeled surface wind speed.

Before entering the discussion of the different modeled species, note the following limitations that apply to the present simulations: (1) As we are only interested in DMS destruction and not so far in its oxidation end products, only a simple DMS oxidation scheme accounting for DMS attack by OH and NO_3 is used. Modeling SO_2 would require accounting for aqueous phase chemistry and heterogeneous reaction on sea salt aerosols, which is postponed to future work (C. Mari et al., manuscript in preparation, 1998). Therefore SO_2 is not discussed in great detail in this paper. (2) No aqueous phase chemistry is treated. This limitation mostly concerns the last of the three Lagrangian flights, as there were little or no clouds in the first two thirds of the experiment. In addition, the species that are mostly concerned by this limitation, that is, SO_2 and HNO_3, are not discussed in this paper and their chemistry has only a very small feedback on the species discussed in this paper, with the exception of peroxide chemistry on flight 26. This point will be discussed later. (3) Photochemical box model caclulations show that nonmethane hydrocarbon chemistry contributes less than 2% to the modeled species discussed here (K. Suhre, unpublished data, 1997). Thus it has not been included for simplicity. (4) Because of the low NO_x concentrations encountered during LB, aircraft measurements of NO display relatively large uncertainties. No NO_2 was observed on the NCAR/C130. Therefore NO_2 and NO_y data from the R/V *Discoverer* have been used. Box model simulations with doubled NO_x concentrations yield an increase in OH of only 15%. Thus uncertainties in NO_x measurements induce an acceptable uncertainty in the modeled OH.

In order to discuss the general features of the diurnal cycles of the different modeled species, their mixing ratios have been averaged over the lowest 1200 m of the MBL (Figures 17a-17d). As can be seen in Figure 17a, roughly half of the NO_2 is photolyzed to NO during
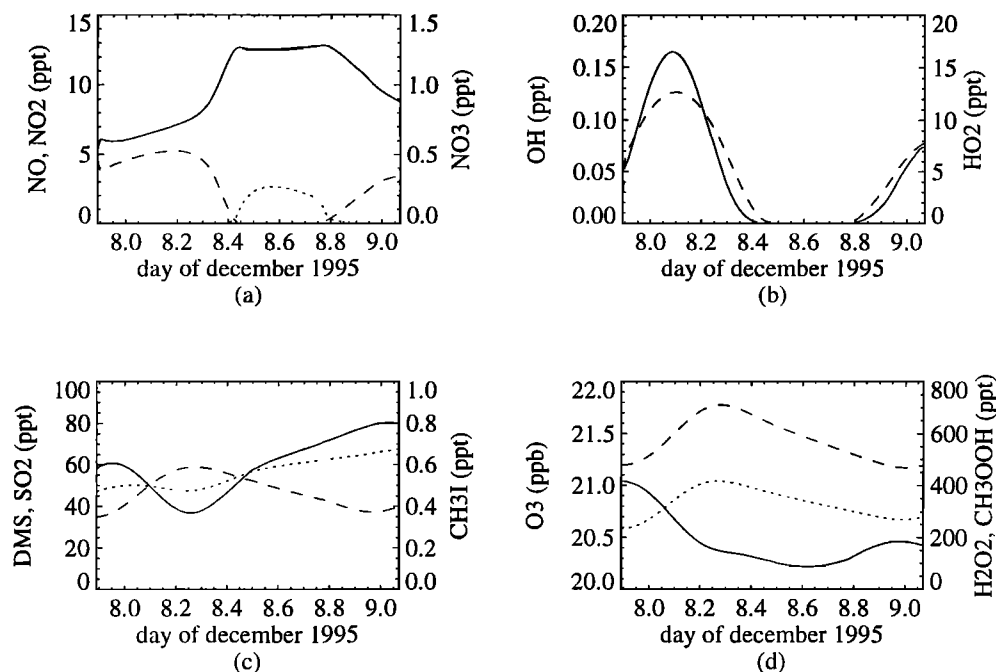
Figure 17. Time series of selected simulated species, averaged between the surface and 1200 m: (a) NO_2 (solid line), NO (dashed line), and NO_3 (dotted line); (b) OH (solid line), and HO_2 (dashed line); (c) DMS (solid line), SO_2 (dashed line), and CH_3I (dotted line); (d) O_3 (solid line), H_2O_2 (dashed line), and CH_3OOH (dotted line). Local night is from day 8.4 to 8.8.

the first (local) day (day of december < 8.4), but much less NO is produced on the second day (day of december > 8.8) due to the presence of clouds, which tend to reduce the average photolysis rates in the MBL. The same effect can be seen for OH and HO_2, which exhibit higher mixing ratios on the first day when no clouds were present (Figure 17b). During the night, NO_3 is formed by reaction of O_3 with NO_2, but with mixing ratios that are too low as to be comparable in magnitude to DMS oxidation by OH during the day. As a consequence, DMS decreases during the first day, followed by an increase at night, which corresponds to the typical DMS diurnal cycle as observed for example in the tropical regions [*Bandy et al.*, 1996; *Suhre et al.*, 1995]. On the second day, DMS continues to increase due to the increasing DMS flux (Figure 17c). The same holds for CH_3I, which has a less pronounced diurnal cycle since it has a longer lifetime than DMS in this situation. The diurnal cycle of SO_2 is inverse to that of DMS, as SO_2 is assumed to be produced from DMS oxidation by OH. An ad hoc SO_2 yield from DMS oxidation by OH of 80% is used, motivated by a similar MSA to non-sea-salt sulphate ratio observed in aerosol ion analysis [*Huebert et al.*, this issue]. Note that *De Bruyn et al.* [this issue] derive a 30-50% SO_2 yield from steady state box model calculations. However, using this lower yield does not significantly impact on any other of the species discussed in this paper. As for SO_2, we find that it increases during the day and decreases during the night when dry deposition dominates its budget. In this case, high wind speeds at the end of LB lead to SO_2 concen-

trations that are not higher on the first day despite the increase in atmospheric DMS concentrations. The diurnal cycles of the peroxides H_2O_2 and CH_3OOH (Figure 17d) resemble those of SO_2, as these peroxides are also mainly produced during daytime. During nighttime, dry deposition dominates, leading to a decrease in peroxides. The ozone mixing ratio does not evolve much during the simulation. During the first day, O_3 is photochemically destroyed, as indicated by a maximal O_3 decay at noon. At night, O_3 is depleted mainly by dry deposition. The increase in model average O_3 before sunrise on the second day is due to vertical transport from above the 1200 m averaging height, as no photochemical O_3 production during the night is possible with the implemented chemical reaction mechanism.

We conclude that the major chemical species simulated here with the 1-D Lagrangian model, averaged over an air column of 1200 m height, behave as one would expect from previous model calculations [e.g., *Thompson et al.*, 1993] and turn now to the discussion of those species for which vertical profiles have been measured. For details concerning the different measurements presented in the respective figures refer to the corresponding experimental papers by J. E. Johnson et al. (unpublished manuscript, 1998) for O_3, F. L. Eisele et al. (unpublished manuscript, 1998) for OH, A. S. H. Prévôt et al. (unpublished manuscript, 1998) for peroxides, A. R. Bandy et al. (unpublished manuscript, 1998) for DMS, and R. R. Blake et al. (unpublished manuscript, 1998) for CH_3I. Additional information on the measurement techniques can also be obtained

from the ACE 1 database via the Codiac interface of the Joint Office for Science Support (UCAR/JOSS, www.joss.ucar.edu).

3.3. Chemistry: O_3

In the unpolluted marine atmosphere at low NO_x levels, ozone has a relatively long photochemical lifetime [Paluch et al., 1995; Noone et al., 1996]. Under these conditions, photochemical ozone production is governed by the reaction of NO with HO_2 (reaction k_4 in appendix) and with CH_3O_2 (k_{14}), which competes with the recombination of NO with O_3 to NO_2 in the photostationary state (J_1, k_{27}, k_{17}). Photochemical ozone loss is dominated by reaction of activated oxygen, $O(^1D)$, with water vapor (k_8) and by reaction of O_3 with HO_2 (k_3). Ozone dry deposition velocities are generally low over the ocean and rate-limited by the surface resistance.

Ozone observations are presented in Figure 8. Significant structure in vertical profiles of ozone has been observed during LB that is very similar to what was encountered during the Atlantic Stratocumulus Transition Experiment/Marine Aerosol and Gas Exchange (ASTEX/MAGE) [Huebert et al., 1996] Lagrangian 1 [Noone et al., 1996, Figures 2 and 3]. Above the MBL, a layer of dry ozone-rich air is found that is attributed to transport from aloft [Newell et al., 1996]. In sounding 24A, a marked jump in ozone mixing ratio in the MBL at about 900 m is observed. In soundings 24X and 24Y, this jump occurs at somewhat lower altitudes, which agrees with a lower altitude of the minor inversion between the upper and lower layer in the MBL in the potential temperature (Figure 2) and water vapor profiles (Figure 3). In sounding 24B, the jump is again at the same altitude as in sounding 24A. Whether this variation in altitude is due to synoptic-scale vertical transport or rather to horizontal inhomogeneity in the Lagrangian air mass is difficult to decide. However, the fact that the model does not see this variation, neither for ozone nor for temperature or humidity (especially in sounding 24Y), despite the fact that it accounts for synoptic-scale subsidence or ascent, favors the latter explanation.

Much of the vertical fine structure in the ozone profiles correlates precisely with the fine structure in the observed water vapor profiles. Examples are an ozone maximum at 700 m that correlates with a minimum in water vapor in sounding 25B, sharp ozone and water vapor gradients at the inversion in soundings 26A and 26B and smoother gradients in sounding 26C, different altitudes of the lower layer on flight 24, and a distinct three-layer structure in sounding 26B. This is consistent with the fact that the ozone decay rate in the MBL at low NO_x levels is approximately proportional to water vapor [Liu et al., 1983; Thompson et al., 1993]. Differences between the modeled and measured ozone profiles are attributed to the fact that the model does not re-

produce the fine structure in the water vapor profile, in particular on flight 26.

Because of its relatively long photochemical lifetime, the effect of vertical synoptic-scale movement is expected to be most visible on the time evolution of the ozone profile. A simulation made without that forcing term is presented in Figure 18. The ozone rich layer that was found in the beginning of LB at 2000 m altitude remains in this case virtually unchanged, whereas the observations and the reference simulation show that it should have weakened and moved upward in the convergent synoptic-scale situation that prevailed after December 8 0600 UTC (see Figure 14b).

3.4. Chemistry: OH

The hydroxyl radical OH is primarily produced by ozone photolysis (J_2), followed by the reaction of water vapor with the activated oxygen atom $O(^1D)$ (k_8). OH oxidizes CH_4 (k_{11}) and CO (k_6) to form the hydroperoxyl radical HO_2, which may be recycled to OH through reaction with NO (k_4). Major HO_x sinks are radical-radical reactions between OH and HO_2. The three factors that control the production of HO_x are thus the ozone and the water vapor mixing ratios and the photolysis rate J_2. The NO_x level controls the partitioning between OH and HO_2.

Figure 9 shows OH concentrations measured during the nine NCAR/C130 aircraft soundings. The first three soundings of flights 24 and 26 have been made at approximately the same local time (24A and 26A at 0720 and 0713 AEST, respectively; 24X/26B at 1027/1015 AEST; 24Y/26C at 1227/1147 AEST). On both days, an OH diurnal cycle was observed, but with a much lower noontime maximum on flight 26 than on flight 24, as can also be seen on the OH time series presented in Figure 19. The 2-σ error of the OH measurements is $\pm42\%$ at pressure levels above 940 mbar and $\pm62\%$ below. Most data points fall within that range around the modeled OH concentrations, although the model tends to give somewhat higher values than the average observed OH concentrations. This may be due to several factors, that is, uncertainty in the NO_x concentrations, horizontal variability in the humidity field
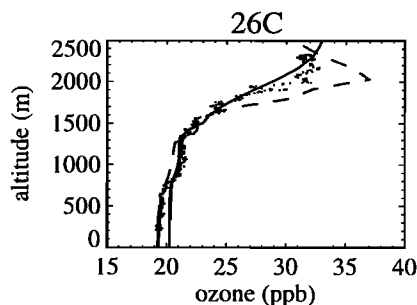
Figure 18. Ozone mixing ratio at the end of LB: data (fine dots), and reference simulation (solid line), without synoptic-scale vertical transport (dashed line).
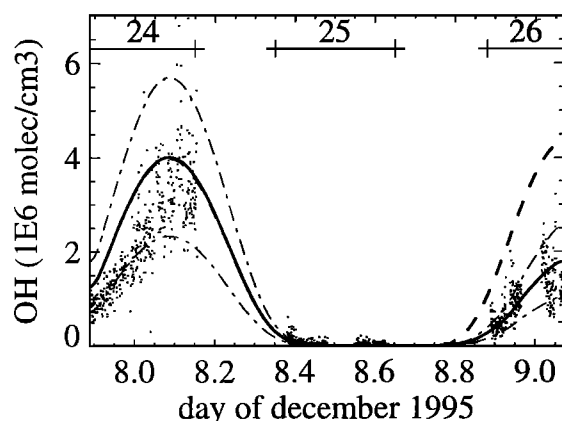
Figure 19. Time series of hydroxyl radical concentration: data taken below 1200 m on aircraft soundings and along horizontal flight legs (dots), simulation with clouds, averaged over the 0-1200 m height range (solid line), ±42% error limits (thin dash-dotted lines), and simulation assuming clear-sky conditions (dashed line). Local night is from day 8.4 to 8.8. Numbers 24-26 indicate the time of the three Lagrangian flights.

(see discussion below), but also uncertainties in the radiative transfer calculations, as there were no photolysis rate measurements made during ACE 1 that would allow for a complete validation of this part of the model (see *Matthijsen et al.* [this issue] for further discussion of this topic).

The lower OH concentrations on the second day (flight 26) are attributed to the presence of clouds on that flight, as a simulation assuming clear-sky conditions confirms (represented by the dashed lines in Figures 9 and 19). For the cloudy simulation (solid line in Figure 9), an altostratus cloud with water content of 0.4 g/kg at 5000 m (as observed by the NCAR/C130 on flight 26 during its descent to the balloons) has been imposed in the calculation of the photolysis rates. Without that high-altitude cloud, the low level clouds would actually have the effect of enhancing photolysis rates above them, leading to even higher OH concentrations than in the clear-sky case (results not shown here). Hence the OH concentrations observed on flight 26 are strongly influenced by the presence of the high-altitude cloud cover. As for the low level clouds, we observe that the modeled OH decreases below each cloud layer, with somewhat enhanced OH in the upper cloud in sounding 26B and 26C, due to enhanced actinic fluxes in the cloud [*Matthijsen et al.*, this issue; *Van Weele and Duynkerke*, 1993]. The decrease in OH concentrations below each cloud layer cannot be identified in the aircraft soundings of flight 26. However, as has been stated earlier, the flight plan was designed in order to minimize encounter of clouds. There have been numerous and vertically more extended cumulus clouds than the soundings on flight 26 would suggest. The model also predicts a deeper cloud cover, so that the modeled OH concentrations are more representing the average situation of flight 26 than the individual soundings. This fact is con-

firmed by Figure 19, which shows all OH observations made below 1200 m, in particular those taken when the aircraft flew horizontal circles and thus sampled the cumulated effect of the numerous cumulus clouds aloft. The observed OH scatters in fact around the modeled OH concentrations on flight 26.

Of particular interest is the OH minimum modeled above the MBL at 1800 m on flight 24 (Figure 9). This minimum can be vaguely identified in the OH measurements in soundings 24A and 24B. It coincides with a minimum in water vapor mixing ratio and a maximum in ozone (both, modeled and observed). A simulation made with ozone increased everywhere by 10% leads to an increase in OH over the entire profile. Hence the ozone maximum cannot be at the origin of the OH minimum. Under clear-sky conditions, the photolysis rates are more or less constant in the noncloudy boundary layer. NO_x, CO, and CH_4 mixing ratios are initialized to vertically constant values, while OH is initialized to zero. In addition, no OH minimum is found in the simulation of flight 26, where there is no humidity minimum in the model either. Thus the OH minimum on flight 24 can only be a consequence of the minimum in the water vapor profile. As we will see next, this OH minimum is then at the origin of a local minimum in the peroxides H_2O_2 and CH_3OOH at that altitude, which was observed for both species in soundings 24A and 24B. Here we can conclude that the model is able to simulate OH vertical profiles that are consistent with humidity and cloud water observations, under cloudy as well as under clear-sky conditions, and that it helps to confirm the existence of an OH minimum above the MBL which is only faintly visible in the observations.

3.5. Chemistry: H_2O_2 and CH_3OOH

The major source of H_2O_2 is the self-reaction of HO_2 (k_7). In the free troposphere, this production is balanced by H_2O_2 photolysis (J_9) and its reaction with OH (k_{10}). H_2O_2 is a very soluble species which reacts easily in the aqueous phase (e.g., with SO_2). We assume that its dry deposition to the ocean is rate-limited by the aerodynamic and laminar resistance (Figure 16). Note that no aqueous phase chemistry is considered here, but this only plays a role during flight 26. For CH_3OOH, the picture is pretty much the same: CH_3OOH is produced by the reaction of HO_2 with CH_3O_2 (k_{23}), and destroyed by photolysis (J_{12}) and reaction with OH (k_{21}, k_{22}). Its dry deposition rate is assumed to be the same as that for H_2O_2. We expect the peroxide production to be largely controlled by the HO_x levels, with decreasing mixing ratio near the surface due to dry deposition.

Figures 10 and 11 display the peroxide mixing ratio observed on the nine NCAR/C130 aircraft soundings. Two simulations are reported in these figures: (1) a simulation using vertically constant initial profiles and (2) a simulation using observed profiles from sounding 24A for initialization and an SST decreased by 3 K after

sounding 25B in order to generate the lowest cold layer observed on flight 26. As already stated above, modeled and measured OH concentrations display a local minimum at 1800 m altitude. The model also predicts a minimum in the HO_2 profile (not shown here). The minima in the measured H_2O_2 and CH_3OOH profiles at the same altitude during flight 24 are thus consistent with the observation of a layer of dry air above the main inversion and a consequence of reduced peroxide production in HO_x poor air. In the lower layer, the peroxides show a strong impact of dry deposition. With increasing wind speed and consequently increasing dry deposition (Figure 16), the peroxide concentrations near the surface decrease, with an increasingly steep, nearly linear profile in the lowest turbulent layer (extending from the surface to 500-800 m). The model reproduces the vertical shape of these profiles in most cases, even on flight 26, when the lowest layer has been forced by lowering the SST. This indicates in particular that the assumed dry deposition velocities for H_2O_2 and CH_3OOH (based on aerodynamic and laminar resistances only) can be used to describe peroxide losses due to surface deposition. Comparison between the simulations, using either vertically homogeneous or observed initial profiles, shows that the model is able to predict the vertical shape of the observed peroxides after a simulation time of 15 hours (sounding 25B), in particular that of CH_3OOH, and this independantly of their initialization. It is interesting to note that the observed peroxide concentrations increase at night between sounding 25A and 25B in the upper layer, a fact that is not reproduced by the model. This might hint at a considerable peroxide nighttime source which deserves further investigation.

### 3.6. Chemistry: DMS and CH_3I

DMS is produced by phytoplankton activity in the ocean. It is the major source of sulfur for the marine atmosphere [*Andreae et al.*, 1985]. DMS is mainly oxidized by OH during the day (k_{36}) and to a minor extent by NO_3 at night (k_{34}). Similar to DMS, CH_3I also has no source in the gas phase and is uniquely emitted by the ocean, where it is produced as a metabolic byproduct of many species of marine algae [*Chameides and Davis*, 1980]. The major CH_3I sink is its photolysis (J_{13}) [*Davis et al.*, 1996]. As no CH_3I seawater measurements were available during ACE 1, we chose to take a CH_3I flux that is proportional to the DMS flux, scaling it with the average ratio between DMS and CH_3I near the surface (in this case, 250). Noontime surface photochemical DMS destruction rates were 3.5×10^{-5} s^{-1} (for OH = 4×10^6 molecules cm^{-3}, reaction rate from *Hynes at al.* [1986]). CH_3I was photolyzed at noon at a rate of 7.3×10^{-6} s^{-1} (absorption cross sections from *Fahr et al.* [1995]). Thus both species are expected to have vertical profiles that decrease with height, DMS decreasing more rapidly and having a more pronounced diurnal cycle than CH_3I due to its shorter lifetime.

Figure 12 shows the DMS mixing ratio observed during LB. No DMS measurements were made during the aircraft soundings. The data presented here were measured when the aircraft flew along constant altitude circles at various levels. Observations that have been taken closer than 1.5 hours to the indicated aircraft sounding are marked by a cross, the remaining data of that flight are denoted by a dot. CH_3I mixing ratio profiles are shown in Figure 13. Measurements made during the aircraft soundings are marked by a cross, and all other data of that flight are denoted by a dot. Although DMS and CH_3I observations have a coarser vertical resolution than, for example, ozone and potential temperature, they still display the two-layer structure of the MBL. The turbulent layer in direct contact with the surface fluxes is characterized by high mixing ratios, whereas lower values prevail in the upper layer. DMS measurements in the free troposphere always revealed near-zero concentrations. Figure 20 shows DMS measurements as a function of time at different altitudes. The DMS diurnal cycle is simulated by the model at different altitudes within the range of scatter in the data. Higher DMS mixing ratios on the second day of LB are due to the increasing DMS fluxes at the end LB, when the DMS air-sea exchange rate was higher due to higher wind speeds.

A major uncertainty in the global sulfur budget resides in the estimate of the global sea-to-air sulfur fluxes [Bates et al., this issue (b)]. As no direct DMS flux measurements are available at present, the DMS flux is in general calculated using global seawater DMS distributions [*Kettle et al.*, 1996] and a parameterization of the DMS exchange coefficient. Note that the LM86 and the W92 parameterizations differ by a factor of more than 2 at high wind speeds, as can be seen in Figure 16. Sim-
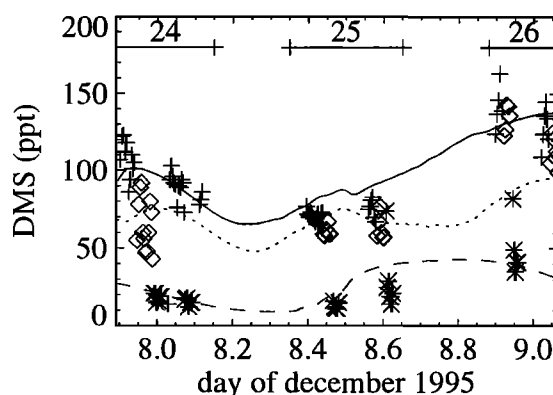
Figure 20. Time series of DMS measured at different altitudes: below 250 m (crosses), between 250 and 500 m (diamonds), between 500 and 1200 m (stars); simulation using the *Liss and Merlivat* [1986] DMS flux parameterization and an SST lowered by 3 K after 15 hours, averaged between 0 and 250 m (solid line), 250 to 500 m (dotted line), and 500 to 1200 m (dashed line). Local night is from day 8.4 to 8.8. Numbers 24-26 indicate the time of the three Lagrangian flights.
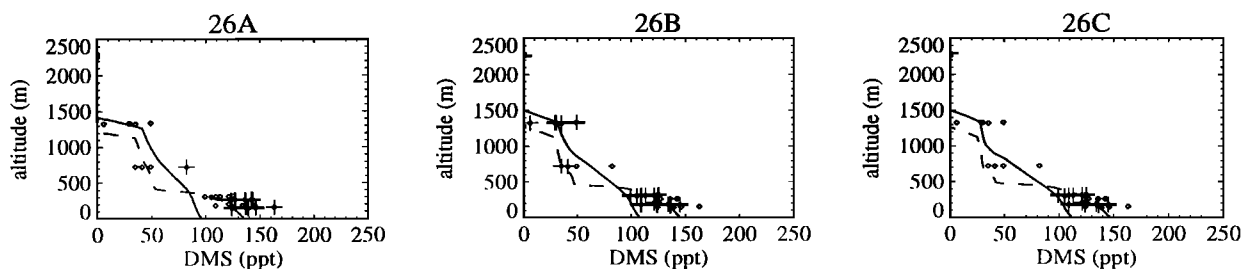
Figure 21. DMS in flight 26: data as in Figure 12, and reference simulation using the *Liss and Merlivat* [1986] DMS flux parameterization (solid line), with SST lowered by 3 K after 15 hours of simulation (dashed line).

ulations with both parameterizations are presented in Figure 12. They clearly show that only the simulations using the LM86 flux parameterization gives consistent results for the first two flights, whereas using W92 yields largely overestimated DMS mixing ratios. As for flight 26, we have seen that the reference simulation fails to reproduce the lowest cold layer on flight 26. This leads to lower DMS mixing ratios, distributed over too large a mixing height. As can be seen in Figure 21, when the model is forced to create that cold layer by decreasing the SST by 3 K after sounding 25B, using the LM86 parameterization leads to improved agreement for flight 26 in the lowest layer. However, agreement in the overlying layer (500-1200 m) appears to be worse in this case as the height where the DMS mixing ratio falls to zero and also the height of the lowermost layer are about 300 m too low. Had the model reproduced these heights correctly, a higher DMS flux would be necessary in order to explain the observations. As no DMS measurements in seawater are available for this last part of the Lagrangian experiment, no further conclusions can be drawn from its discussion. Therefore we will restrict ourselves in the following to the first two Lagrangian flights (24 and 25).

What are the uncertainties in these model calculations? DMS seawater concentrations are constrained by direct measurements on the R/V *Discoverer* until sounding 25B, so that DMS seawater concentrations present a major uncertainty only for the simulation of flight 26. As shown above, OH concentrations agree with the measurements within the range of observational errors, although OH is somewhat overestimated by the model in soundings 24X and 24B. A correction of this bias toward lower OH concentrations would lead to lower DMS oxidation rates, thus favoring the lower DMS flux estimate (LM86). The vertical turbulent structure of the MBL (Figure 7), as well as surface wind speeds (Figure 5) are correctly modeled for flights 24 and 25. As opposed to a box model approach, no supplementary assumptions on the mixing height or entrainment rates are made here, and any DMS advection is excluded by the Lagrangian reference frame. Hence, we conclude that only when using the LM86 parameterization can we model DMS concentrations correctly.

This conclusions is, however, based on the assumption that OH and NO_3 radicals are the only significant DMS oxidants. Any additional atmospheric DMS sink would require a respectively higher DMS ocean source. The existence of such an additional DMS oxidant is supported by some, but not all recent atmospheric DMS measurements in other parts of the world [*Chin et al.*, 1998; *Bandy et al.*, 1996; *Yvon et al.*, 1996; *Suhre et al.*, 1995]. It has been suggested recently that Cl radicals [*Keene et al.*, 1996] and some bromine-containing compounds (Br and BrO) released from aerosols [*Sander and Crutzen*, 1996] may also be important DMS oxidants. While possibly important in polluted atmospheres, there is at present no direct evidence for any significance in the remote marine atmosphere. Such an additional DMS oxidant would require the DMS diurnal cycle to be more pronounced than the one modeled here. This would still be within the variability of the observations presented in Figure 20. Moreover, recent studies show that organic films may play an important role in air-sea gas exchange [*Frew*, 1997]. We should be clear about the fact that both DMS flux parameterizations used here (LM86 and W92) are a function of wind speed and the sea-air DMS gradient only.

For a full understanding of the fate of atmospheric DMS, it will eventually be necessary to model the fate of its oxidation products, in particular that of SO_2 and MSA. Unfortunately, there is still much uncertainty here as well, in particular in what concerns the DMS degradation mechanism and thus the SO_2 yield [*Capaldo and Pandis*, 1997], and also the fate of SO_2 itself, that is, its oxidation in sea-salt aerosols and cloud droplets [*Sievering et al.*, 1992, also unpublished manuscript 1998; *O'Dowd et al.*, 1997]. However, for the interested reader we present in Figure 22 a comparison between SO_2 observed in the lowest 0-500 m and SO_2 modeled with a 0.8 yield from DMS oxidation, but ignoring all heterogeneous processes such as in-cloud oxidation and loss on sea-salt aerosols. Dry deposition is parameterized as described above for H_2O_2. The initial profile is constant with a SO_2 mixing ratio of 35 ppt. It can be seen that heterogeneous SO_2 loss cannot be neglected on flights 25 and 26, during which clouds were present and sea-spray aerosol generation was high due
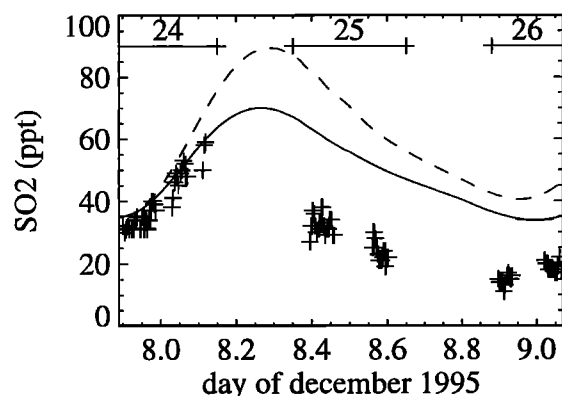
Figure 22. Time series of SO_2 measured below 500 m (crosses); reference simulation using the *Liss and Merlivat* [1986] DMS flux parameterization, averaged between 0 and 500 m (solid line), and simulation with *Wanninkhof* [1992] DMS flux parameterization (dashed line). Local night is from day 8.4 to 8.8. Numbers 24-26 indicate the time of the three Lagrangian flights.

to high surface winds. This agrees with the fact that SO_2 is overestimated by the model during these last two flights. Flight 24, in contrast, took place under cloud-free conditions with low surface winds ($\approx$5 m/s). Here, heterogeneous processes can be assumed to be of minor importance, so that we can draw some conclusions from the agreement between the modeled and observed SO_2 increase in the beginning of the Lagrangian experiment. Had we used an SO_2 yield of 0.3-0.5 as proposed by *De Bruyn et al.* [this issue] instead of 0.8, as inspired from the MSA to non-sea-salt sulphate ratio observed in aerosol ion analysis [Huebert et al., this issue], we could explain only half of the observed SO_2 increase with our model. In this case, we would need an extra SO_2 source and thus potentially an extra DMS oxidation pathway.
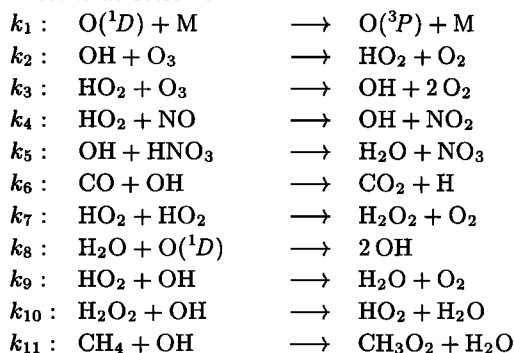
4. Conclusions

A major objective of this work is to investigate to what degree a one-dimensional Lagrangian boundary layer meteorological model with coupled gas phase photochemistry is able to reproduce the time evolution and the vertical distribution of basic reactive species, which were observed during the ACE 1 Lagrangian experiment B (LB). This question was answered mostly positively by direct comparison of modeled profiles with observed profiles of different reactive species from nine Lagrangian aircraft soundings. The crucial point was to reproduce the dynamical structure of the marine boundary layer with the model, which was possible during the first two Lagrangian flights, but turned out to be more difficult during the third flight, when, after 24 hours from the beginning of the experiment, scattered cumulus clouds formed and the boundary layer become devided in up to three vertical layers. A very sensitive parameter in the present situation turned out to be the sea surface temperature, being the controlling factor in the generation of turbulence.
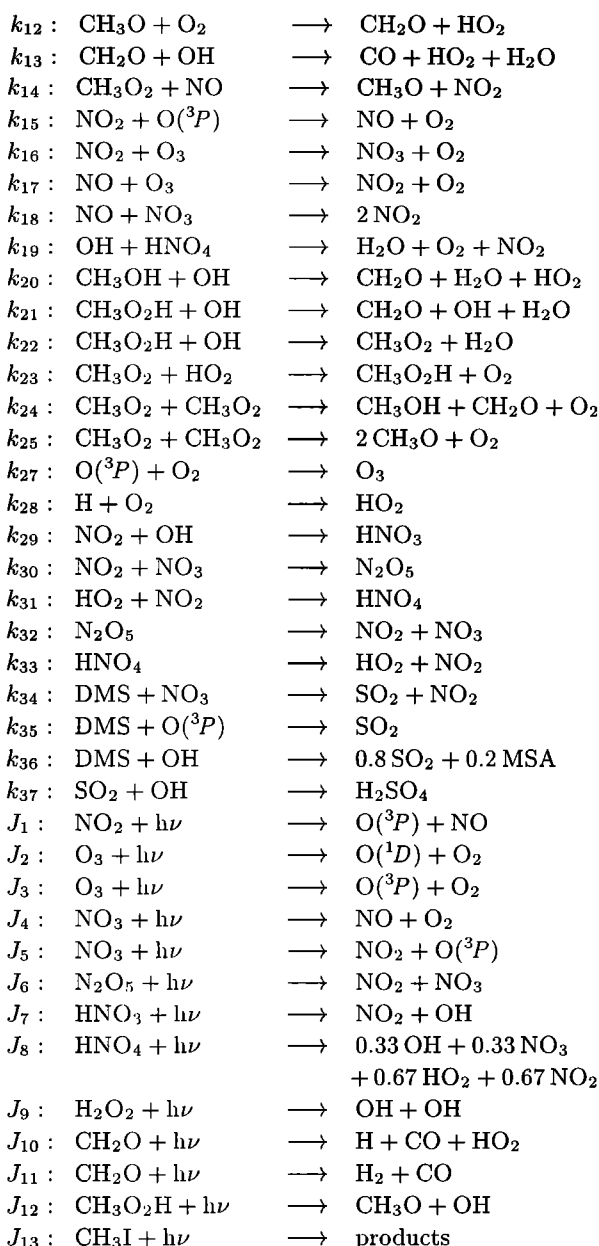
In contrast to a simple box model, the 1-D model allows for a much more detailed physical representation of boundary layer processes and their impact on chemistry, in particular with regard to noninstantaneous vertical turbulent mixing, layered vertical structure, and cloud processes. No assumption about mixing heights or entrainment rates are required in this type of model. In this context, a number of conclusions were drawn: (1) Ozone, having a relatively long photochemical lifetime in the clean marine boundary layer, was most sensitive to vertical transport processes, in particular to vertical synoptic-scale transport. (2) The model is able to "create" the vertical structure of the observed peroxides from initally constant vertical profiles, emphasizing the internal coherence of the modeling system. (3) OH concentrations were in agreement with observations, both on cloudy and noncloudy days. On the first flight, a layer of dry ozone rich air topped the boundary layer. The model consistently predicted a minimum in OH and peroxides at that altitude that was also observed. (4) The most interesting result with regard to the ACE 1 objectives concerns the parameterization of the DMS flux: we find that agreement in the modeling of atmospheric DMS can only be reached when using the LM86 flux parameterization, assuming that OH is the only major DMS oxidant. Refer also to the companion paper [*Mari et al.*, this issue] for a three-dimensional study of DMS emission, transport and oxidation at the mesoscale, which draws similar conclusions on a more regional scale. As for CH_3I, seawater measurements would be necessary to validate its simulation.

Here, only the effect of clouds on photolysis rates was considered. With respect to the objectives of ACE 1, that is, the determination of the key physical and chemical processes controlling the formation and evolution of aerosols, the next step is to include aerosol and cloud phase chemistry into the present simulation. This will allow for the study of SO_2 and sulfate aerosol formation and growth, constraining the model with Lagrangian measurements of aerosol microphysical, chemical, and optical properties, as well as gas phase MSA and H_2SO_4 concentrations that are all available for ACE 1 Lagrangian B.

Appendix

The reaction mechanism implemented in the 1-D model is as follows.

k_1 :	$O(^1D) + M$	$\longrightarrow$	$O(^3P) + M$
k_2 :	$OH + O_3$	$\longrightarrow$	$HO_2 + O_2$
k_3 :	$HO_2 + O_3$	$\longrightarrow$	$OH + 2O_2$
k_4 :	$HO_2 + NO$	$\longrightarrow$	$OH + NO_2$
k_5 :	$OH + HNO_3$	$\longrightarrow$	$H_2O + NO_3$
k_6 :	$CO + OH$	$\longrightarrow$	$CO_2 + H$
k_7 :	$HO_2 + HO_2$	$\longrightarrow$	$H_2O_2 + O_2$
k_8 :	$H_2O + O(^1D)$	$\longrightarrow$	$2OH$
k_9 :	$HO_2 + OH$	$\longrightarrow$	$H_2O + O_2$
k_{10} :	$H_2O_2 + OH$	$\longrightarrow$	$HO_2 + H_2O$
k_{11} :	$CH_4 + OH$	$\longrightarrow$	$CH_3O_2 + H_2O$

k_{12} : $CH_3O + O_2$ $\longrightarrow$ $CH_2O + HO_2$

k_{13} : $CH_2O + OH$ $\longrightarrow$ $CO + HO_2 + H_2O$

k_{14} : $CH_3O_2 + NO$ $\longrightarrow$ $CH_3O + NO_2$

k_{15} : $NO_2 + O(^3P)$ $\longrightarrow$ $NO + O_2$

k_{16} : $NO_2 + O_3$ $\longrightarrow$ $NO_3 + O_2$

k_{17} : $NO + O_3$ $\longrightarrow$ $NO_2 + O_2$

k_{18} : $NO + NO_3$ $\longrightarrow$ $2\,NO_2$

k_{19} : $OH + HNO_4$ $\longrightarrow$ $H_2O + O_2 + NO_2$

k_{20} : $CH_3OH + OH$ $\longrightarrow$ $CH_2O + H_2O + HO_2$

k_{21} : $CH_3O_2H + OH$ $\longrightarrow$ $CH_2O + OH + H_2O$

k_{22} : $CH_3O_2H + OH$ $\longrightarrow$ $CH_3O_2 + H_2O$

k_{23} : $CH_3O_2 + HO_2$ $\longrightarrow$ $CH_3O_2H + O_2$

k_{24} : $CH_3O_2 + CH_3O_2$ $\longrightarrow$ $CH_3OH + CH_2O + O_2$

k_{25} : $CH_3O_2 + CH_3O_2$ $\longrightarrow$ $2\,CH_3O + O_2$

k_{27} : $O(^3P) + O_2$ $\longrightarrow$ O_3

k_{28} : $H + O_2$ $\longrightarrow$ HO_2

k_{29} : $NO_2 + OH$ $\longrightarrow$ HNO_3

k_{30} : $NO_2 + NO_3$ $\longrightarrow$ N_2O_5

k_{31} : $HO_2 + NO_2$ $\longrightarrow$ HNO_4

k_{32} : N_2O_5 $\longrightarrow$ $NO_2 + NO_3$

k_{33} : HNO_4 $\longrightarrow$ $HO_2 + NO_2$

k_{34} : $DMS + NO_3$ $\longrightarrow$ $SO_2 + NO_2$

k_{35} : $DMS + O(^3P)$ $\longrightarrow$ SO_2

k_{36} : $DMS + OH$ $\longrightarrow$ $0.8\,SO_2 + 0.2\,MSA$

k_{37} : $SO_2 + OH$ $\longrightarrow$ H_2SO_4

J_1 : $NO_2 + h\nu$ $\longrightarrow$ $O(^3P) + NO$

J_2 : $O_3 + h\nu$ $\longrightarrow$ $O(^1D) + O_2$

J_3 : $O_3 + h\nu$ $\longrightarrow$ $O(^3P) + O_2$

J_4 : $NO_3 + h\nu$ $\longrightarrow$ $NO + O_2$

J_5 : $NO_3 + h\nu$ $\longrightarrow$ $NO_2 + O(^3P)$

J_6 : $N_2O_5 + h\nu$ $\longrightarrow$ $NO_2 + NO_3$

J_7 : $HNO_3 + h\nu$ $\longrightarrow$ $NO_2 + OH$

J_8 : $HNO_4 + h\nu$ $\longrightarrow$ $0.33\,OH + 0.33\,NO_3$
$+ 0.67\,HO_2 + 0.67\,NO_2$

J_9 : $H_2O_2 + h\nu$ $\longrightarrow$ $OH + OH$

J_{10} : $CH_2O + h\nu$ $\longrightarrow$ $H + CO + HO_2$

J_{11} : $CH_2O + h\nu$ $\longrightarrow$ $H_2 + CO$

J_{12} : $CH_3O_2H + h\nu$ $\longrightarrow$ $CH_3O + OH$

J_{13} : $CH_3I + h\nu$ $\longrightarrow$ products

Reaction rates, absorption cross sections, and quantum yields are as in *DeMore et al.* [1992]. CH_3I absorption cross sections are from *Fahr et al.* [1995]. The following 23 species are treated prognostically: O_3, $O(^1D)$, $O(^3P)$, NO, NO_2, NO_3, N_2O_5, HNO_3, HNO_4, H_2O_2, OH, HO_2, H, CO, CH_4, CH_2O, CH_3OH, CH_3O_2H, CH_3O_2, CH_3O, SO_2, DMS, and CH_3I.

References

Ackerman, A. S., O. B. Toon, and P. Hobbs, A model for particle microphysics, turbulent mixing, and radiative transfer in the stratocumulus-topped marine boundary layer and comparisons with measurements, *J. Atmos. Sci.*, *52*, 1204-1236, 1995.

Andreae, M. O., R. J. Ferek, F. Bermond, K. P. Byrd, R. T. Engstrom, S. Hardin, P. D. Houmere, F. LeMarrec, and H. Raemdonck, Dimethyl sulfide in the marine atmosphere, *J. Geophys. Res.*, *90*, 12891-12900, 1985.

Baer, M., and K. Nester, Parameterization of trace gas dry deposition velocities for a regional mesoscale diffusion model, *Ann. Geophys.*, *10*, 912-923, 1992.

Bandy, A. R., D. C. Thornton, B. W. Blomquist, S. Chen, T. P. Wade, J. C. Ianni, G. M. Mitchell, and W. Nadler, Chemistry of dimethylsulfide in the equatorial Pacific atmosphere, *Geophys. Res. Lett.*, *23*, 741-744, 1996.

Bates, T. S., B. J. Huebert, J. L. Gras, B. Griffiths, and P. A. Durkee, The International Global Atmospheric Chemistry (IGAC) Project's First Aerosol Characterization Experiment (ACE 1): Overview, *J. Geophys. Res.*, this issue (a).

Bates, T. S., V. N. Kapustin, P. K. Quinn, D. S. Covert, D. J. Coffman, C. Mari, P. A. Durkee, W. J. De Bruyn, and E. S. Saltzman, Processes controlling the distribution of aerosol particles in the lower marine boundary layer during ACE 1, *J. Geophys. Res.*, this issue, (b).

Bechtold, P., C. Fravalo, and J. P. Pinty, A model of marine boundary layer cloudiness for mesoscale applications, *J. Atmos. Sci.*, *49*, 1723-1744, 1992.

Bechtold, P., S. K. Krueger, W. S. Lewellen, E. van Meijgard, C.-H. Moeng, D. A. Randall, A. van Ulden, and S. Wang, Modeling a stratocumulus-topped PBL: Intercomparison among different one-dimensional code with large eddy simulation, *Bull. Am. Meteorol. Soc.*, *77*, 2033-2042, 1996.

Bougeault, P., and P. Lacarrère, Parameterization of orography-induced turbulence in a meso-beta model, *Mon. Weather Rev.*, *117*, 1872-1890, 1989.

Bretherton, C. S., S. K. Krueger, M. C. Wyant, P. Bechtold, E. van Meijgaard, B. Stevens, and J. Teixeira, A GCSS boundary layer model intercomparison study of the first ASTEX Lagrangian experiment, *Boundary Layer Meteorol.*, in press, 1998.

Businger, S., S. R. Chiswell, W. C. Ulmer, and R. Johnson, Balloons as a Lagrangian measurement platform for atmospheric research, *J. Geophys. Res.*, *101*, 4363-4376, 1996.

Capaldo, K. P., and S. N. Pandis, Dimethylsulfide chemistry in the remote marine atmosphere: Evaluation and sensitivity analysis of available mechanisms, *J. Geophys. Res.*, *102*, 23251-23267, 1997.

Chameides, W. L., and D. D. Davis, Iodine: Its possible role in tropospheric photochemistry, *J. Geophys. Res.*, *85*, 7383-7398, 1980.

Charnock, H., Wind stress on a water surface, *Q. J. R. Meteorol. Soc.*, *81*, 639, 1955.

Chin, M., R. B. Rood, D. J. Allen, M. O. Andreae, A. M. Thompson, S.-J. Lin, R. M. Atlas, and J. V. Ardizzone,

Processes controlling dimethyl sulfide over the ocean: Case studies using a 3-D model driven by assimilated meteorological fields, *J. Geophys. Res.*, in press, 1998.

Davis, D., J. Crawford, S. Liu, S. McKeen, A. R. Bandy, D. C. Thornton, F. Rowland, and D. R. Blake, Potential impact of iodine on tropospheric levels of ozone and other critical oxidants, *J. Geophys. Res.*, *101*, 2135–2147, 1996.

De Bruyn, W. J., T. S. Bates, J. M. Cainey, and E. S. Saltzman, Shipboard measurements of DMS and SO_2 southwest of Tasmania during ACE 1, *J. Geophys. Res.*, this issue.

DeMore, W. B., S. P. Sander, D. M. Golden, R. F. Hampson, M. J. Kurylo, C. J. Howard, A. R. Ravishankara, C. E. Kolb, and M. J. Molina, Chemical kinetics and photochemical data for use in stratospheric modeling, Evaluation number 10, *JPL Pub., 92-20*, 1992.

Fahr, A., A. K. Nayak, and M. J. Kurylo, The ultraviolet absorption cross section of CH_3I, temperature dependant gas and liquid phase measurements, *Chem. Phys., 197*, 195–203, 1995.

Fouquart, J., C. Buriez, M. Herman, and R. S. Kandel, The influence of clouds on radiation: A climate-modeling perspective, *Rev. Geophys., 28*, 145–166, 1990.

Frew, N. M., The role of organic films in air-sea gas exchange, in *The Sea Surface and Global Change*, edited by P. S. Liss and R. A. Duce, pp. 121–171, Cambridge Univ. Press, New York, 1997.

Gabric, A. J., G. P. Ayers, and C. Sander, Independent marine and atmospheric model estimates of the sea-air flux of dimethylsulfide in the Southern Ocean, *Geophys. Res. Lett., 22*, 3521–3524, 1995.

Haltiner, G. J., and R. T. Williams, *Numerical Prediction and Dynamical Meteorology*, John Williams, New York, 1980.

Huebert, B. J., A. A. Pszenny, and B. Blomquist, The AS-TEX/MAGE Experiment, *J. Geophys. Res., 101*, 4319–4329, 1996.

Huebert, B. J., S. G. Howell, L. Zhuang, J. Heath, M. Litchy, D. J. Wylie, J. Kreidler, S. Coeppicus, and J. Pfeiffer, Filter and impactor measurements of anions and cations during ACE 1, *J. Geophys. Res.*, this issue.

Hynes, A. J., P. J. Wine, and D. H. Semmes, Kinetics and mechanism of OH reactions with organic sulfides, *J. Phys. Chem., 90*, 4148–4156, 1986.

Keene, W. C., D. J. Jacob, and S. M. Fan, Reactive chlorine - A potential sink for dimethylsulfide and hydrocarbons in the marine boundary layer, *Atmos. Environ., 30*, R1–R3, 1996.

Kessler, E., On the distribution and continuity of water substance in atmospheric circulations, *Meteorol. Monogr., 10*(32), 84 pp., 1969.

Kettle, A. J., M. O. Andreae, D. Amouroux, G. Helas, S. Rapsomanikis, G. Roberts, G. Schebeske, and G. Uher, A preliminary global database of sea surface dimethyl sulfide measurements and a simple model to predict sea surface dimethyl sulfide as a function of latitude, longitude, and month, *EOS Trans. AGU, 77*(46), Fall Meet. Suppl., 417, 1996.

Kok, G. L., A. S. H. Prévôt, R. D. Schillawski and J. E. Johnson, Carbon monoxide measurements from 76°N to 59°S and over the South Tasman Sea, *J. Geophys. Res.*, this issue.

Lafore, J. P., et al., The Meso-NH Atmospheric Simulation System, I, Adiabatic formulation and control simulations, *Ann. Geophys., 16*, 90-109, 1998.

Liss, P. S., and L. Merlivat, Air-sea gas exchange rates: Introduction and synthesis, in *The Role of Air-Sea Exchange in Geochemical Cycling*, edited by P. Buat-Menard, pp. 113–127, D. Reidel, Norwell, Mass., 1986.

Liu, S. C., M. McFarland, D. Kley, O. Zafiriou, and B. Huebert, Tropospheric NO_x and O_3 budgets in the equatorial Pacific, *J. Geophys. Res., 88*, 1360–1368, 1983.

Madronich, S., and G. Weller, Numerical integration errors in calculated tropospheric photodissociation rate coefficients, *J. Atmos. Sci., 10*, 289–300, 1990.

Mari, C., K. Suhre, T. S. Bates, J. E. Johnson, R. Rosset, A. R. Bandy, F. L. Eisele, R. L. Mauldin III, and D. C. Thornton, Physico-chemical modeling of ACE 1 Lagrangian B, 2, DMS emission, transport, and oxidation at the mesoscale, *J. Geophys. Res.*, this issue.

Matthijsen J., K. Suhre, R. Rosset, F. L. Eisele, R. L. Mauldin III, and D. J. Tanner, Photodissociation and UV-radiative transfer in a cloudy atmosphere: Modeling and measurements, *J. Geophys. Res.*, this issue.

Morcrette, J.-J., Impact of changes of the radiation transfer parameterisations plus cloud optical properties in the ECMWF model, *Mon. Weather Rev., 118*, 847–873, 1989.

Newell, R. E., Z.-X. Wu, Y. Zhu, W. Hu, E. V. Browell, G. L. Gregory, G. W. Sachse, J. E. Collins Jr., K. K. Kelly, and S. C. Liu, Vertical fine-scale atmospheric structure measured from NASA DC-8 during PEM-West A, *J. Geophys. Res., 101*, 1943–1960, 1996.

Nickerson, E. C., E. Richard, R. Rosset, and D. R. Smith, The numerical simulation of clouds, rain, and airflow over the Vosges and Black Forest mountains: A meso-β model with parameterized microphysics, *Mon. Weather Rev., 114*, 398–414, 1986.

Noone, K. J., R. D. Schillawski, G. L. Kok, C. S. Bretherton, and B. Huebert, Ozone in the marine atmosphere observed during the Atlantic Stratocumulus Transition Experiment/ Marine Aerosol and Gas Exchange, *J. Geophys. Res., 101*, 4485–4499, 1996.

O'Dowd, C. D., M. H. Smith, I. E. Consterdine, and J. A. Lowe, Marine aerosol, sea-salt, and the marine sulphur cycle: A short review, *Atmos. Environ., 31*, 73–80, 1997.

Paluch, I. R., S. McKeen, D. H. Lenschow, R. D. Schillawski, and G. L. Kok, Evolution of the subtropical marine boundary layer: Photochemical ozone loss, *J. Atmos. Sci., 52*, 2967–2976, 1995.

Petropavlovskikh, I. V., Evaluation of photodissociation coefficient calculations for use in atmospheric chemical models, Ph.D. thesis, Univ. Libre de Bruxelles, Bruxelles, Belgium, 1995.

Quinn, P. K., T. L. Anderson, T. S. Bates, R. Dlugi, J. Heintzenberg, W. von Hoyingen-Huene, M. Kulmala, P. B. Russell, and E. Sweitlicki, Closure in tropospheric aerosol-climate research: A review and future needs for addressing aerosol direct short-wave radiative forcing, *Contrib. Atmos. Phys., 69*, 547–577, 1996.

Ramaroson, R., M. Pirre, and D. Cariolle, A box model for on-line computations of diurnal variations in a 1-D model: potential for application in multidimensional cases, *Ann. Geophys., 10*, 416–428, 1992.

Redelsperger, J. L., and G. Sommeria, Méthode de représentation de la turbulence d'échelle inférieure à la maille pour un modèle tri-dimensionnel de convection nuageuse, *Boundary Layer Meteorol., 21*, 509–530, 1981.

Sander, R., and P. J. Crutzen, Model study indicating halogen activation and ozone destruction in polluted air masses transported to the sea, *J. Geophys. Res., 101*, 9121–9138, 1996.

Sievering, H., J. Boatman, E. Gorman, Y. Kim, L. Anderson, G. Ennis, M. Luria, and S. Pandis, Removal of sulphur from the marine boundary layer by ozone oxidation in sea salt aerosols, *Nature, 360*, 571–573, 1992.

Stull, R. B., *An Introduction to Boundary Layer Meteorology*, Kluwer Acad., Norwell, Mass., 1988.

Suhre, K., and R. Rosset, DMS oxidation and turbulent

transport in the marine boundary layer: A numerical study, *J. Atmos. Chem.*, *18*, 379–395, 1994a.

Suhre, K., and R. Rosset, Modification of a linearized semi-implicit scheme for chemical reactions using a steady-state-approximation, *Ann. Geophys.*, *12*, 359–361, 1994b.

Suhre, K., M. O. Andreae, and R. Rosset, Biogenic sulfur emissions and aerosols over the tropical South Atlantic, 2, One-dimensional simulation of sulfur chemistry in the marine boundary layer, *J. Geophys. Res.*, *100*, 11323–11334, 1995.

Thompson, A. M., et al., Ozone observations and a model of marine boundary layer photochemistry during SAGA 3, *J. Geophys. Res.*, *98*, 16955–16968, 1993.

Toon, O. B., C. P. McKay, and T. P. Ackerman, Rapid calculation of radiative heating rates and photodissociation rates in inhomogeneous multiple scattering atmospheres, *J. Geophys. Res.*, *94*, 16287–16301, 1989.

Van Weele, M., and P. G. Duynkerke, Effect of clouds on the photodissociation of NO_2: observations and modelling, *J. Atmos. Chem.*, *16*, 231–255, 1993.

Wang, Q., and P. Linlin, Boundary layer evolution in response to variations of sea surface temperature and wind shear, paper presented at the 12th Symposium on Boundary Layers and Turbulence, Am. Meterol. Soc., Vancouver, Canada, 1997.

Wanninkhof, R., Relationship between wind speed and gas exchange over the ocean, *J. Geophys. Res.*, *97*, 7373–7382, 1992.

Yvon, S. A., E. S. Saltzman, D. J. Cooper, T. S. Bates, and A. M. Thompson, Atmospheric sulfur cycling in the tropical Pacific marine boundary layer (12°S, 135°W): A comparison of field sata and model results. 1. Dimethyl-sulfide, *J. Geophys. Res.*, *101*, 6899–6909, 1996.

A. R. Bandy and D. C. Thornton, Department of Chemistry, Drexel University, Philadelphia, PA 19104.

T. S. Bates and J. E. Johnson, Pacific Marine Environmental Laboratory/NOAA, Seattle, WA 98115.

D. R. Blake, Department of Chemistry, University of California at Irvine, Irvine, CA 92717.

S. Businger, Department of Meteorology, University of Hawai'i at Mānoa, Honolulu, HI 96822.

F. L. Eisele, L. Mauldin III, and D. J. Tanner, ACD, NCAR, Boulder, CO 80307.

B. J. Huebert, Department of Oceanography, University of Hawai'i at Mānoa, Honolulu, HI 96822.

G. L. Kok and R. D. Schillawski, RAF, NCAR, Boulder, CO 80307.

C. Mari, R. Rosset, K. Suhre, Laboratoire d'Aérologie, UMR CNRS/UPS 5560, 31400 Toulouse, France. (e-mail: suhk@aero.obs-mip.fr)

A. S. H. Prévôt, Paul Scherrer Institute, 5232 Villigen-PSI, Switzerland.

Q. Wang, Naval Postgraduate School, Monterey, CA 93943.